How thermochemical piles can (periodically) generate plumes at their edges

Björn H. Heyn [1], Clinton P. Conrad [1], Reidar G. Trønnes [1,2]

[1]Centre for Earth Evolution and Dynamics (CEED), University of Oslo, Norway

[2]Natural History Museum, University of Oslo, Norway

Key Points:

- Plumes can be periodically generated at the margins of thermochemical piles by local pile collapse
- Variations in pile thickness and lateral motion of the pile edge reflect cycles of plume initiation
- The period of plume cycles is controlled by plate velocity and the sinking rate of slabs

Corresponding author: Björn H. Heyn, b.h.heyn@geo.uio.no

This article has been accepted for publication and undergone full peer review but has not been through the copyediting, typesetting, pagination and proofreading process which may lead to differences between this version and the Version of Record. Please cite this article as doi: 10.1029/2019JB018726

Abstract

Deep-rooted mantle plumes are thought to originate from the margins of the Large Low Shear Velocity Provinces (LLSVPs) at the base of the mantle. Visible in seismic tomography, the LLSVPs are usually interpreted to be intrinsically dense thermochemical piles in numerical models. Although piles deflect lateral mantle flow upwards at their edges, the mechanism for localized plume formation is still not well understood. In this study, we develop numerical models that show plumes rising from the margin of a dense thermochemical pile, temporarily increasing its local thickness until material at the pile top cools and the pile starts to collapse back towards the core-mantle boundary (CMB). This causes dense pile material to spread laterally along the CMB, locally thickening the lower thermal boundary layer on the CMB next to the pile, and initiating a new plume. The resulting plume cycle is reflected in both the thickness and lateral motion of the local pile margin within a few hundred km of the pile edge, while the overall thickness of the pile is not affected. The period of plume generation is mainly controlled by the rate at which slab material is transported to the CMB, and thus depends on the plate velocity and the sinking rate of slabs in the lower mantle. A pile collapse, with plumes forming along the edges of the pile's radially extending corner, may for example explain the observed clustering of Large Igneous Provinces (LIPs) in the southeastern corner of the African LLSVP around 95-155 Ma.

Plain Language Summary

Deep-rooted upwellings in the Earth's mantle, so-called "plumes", are responsible for volcanism such as Hawaii and seem to cluster around two continent-sized regions at the core-mantle boundary that show anomalously low seismic velocities. These regions have been suggested to have a different composition than the surrounding mantle, causing them to be denser and stiffer which allows them survive billions of years at the base of the mantle without being completely eroded. In this study, we use numerical simulations to show that mantle plumes and dense piles at the core-mantle boundary interact with each other, potentially resulting in a periodic plume initiation. A starting upwelling increases the pile thickness locally by pulling dense pile material upward. It then cools down, causing a density increase that results in gravitational collapse of the dense material towards the core-mantle boundary. As a result, this material spreads along the boundary and pushes hot ambient mantle in front of it, thereby triggering a new upwelling, and the cycle starts from the beginning. The main control on how often upwellings are generated is the rate at which material from subduction zones at the Earth's surface reaches the core-mantle boundary, which relates to the velocity of tectonic plates.

1 Introduction

All seismic tomography models throughout the last decades show a similar degree-2 pattern for the Earth's lowermost mantle (e.g., Hager et al., 1985; Dziewonski et al., 2010; Garnero et al., 2016), dominated by the presence of two so-called Large Low Shear Velocity Provinces (LLSVPs) (Garnero & McNamara, 2008; Dziewonski et al., 2010; Garnero et al., 2016) centered beneath Africa and the Pacific (Garnero & McNamara, 2008; Lekic et al., 2012; Cottaar & Lekic, 2016). Although the various tomographic models suggest slightly different shapes and thicknesses of these structures, there is in general good agreement about the positions of their outlines (Cottaar & Lekic, 2016). Hotspots related to deep-roted plumes seem to be located at the LLSVP margins (French & Romanowicz, 2015; Torsvik et al., 2016), even though the statistical correlation is still under discussion (Austermann et al., 2014; Davies et al., 2015; Doubrovine et al., 2016). Although some studies suggest that they may be simple accumulations of thermal plumes swept together by mantle flow (e.g., Schuberth, Bunge, Steinle-Neumann, et al., 2009; Schuberth, Bunge, & Ritsema, 2009; Schuberth et al., 2012; Davies et al., 2012), most studies assume and favor a thermochemical origin of the LLSVP structures, in which they represent piles of hot and dense material (e.g., McNamara & Zhong, 2004, 2005; Nakagawa & Tackley, 2011; Tackley, 2012; Y. Li et al., 2014, 2015; Mulyukova et al., 2015).

If the LLSVPs (mostly) consist of intrinsically denser material, they are hypothesized to be composed of either recycled oceanic crust, including mid-ocean ridge basalt (Christensen & Hofmann, 1994; Hirose et al., 2005; M. Li & McNamara, 2013; M. Li et al., 2014; Mulyukova et al., 2015) or iron-rich cumulates (McNamara & Zhong, 2004, 2005; Nakagawa & Tackley, 2011; Y. Li et al., 2014, 2015) that crystallized at a relatively late stage from the basal magma ocean (BMO, Labrosse et al., 2007). Such thermochemical piles may be largely confined to the lowermost 300 km above the core-mantle boundary (CMB), where most S-wave tomography models show large amplitudes of velocity variation (Romanowicz, 2003; Lay, 2015). Constraints on the total excess density of thermochemical LLSVPs (including both thermal and chemical effects) have been obtained through the analysis of normal modes (Koelemeijer et al., 2017), Earth's solid tides (Lau et al., 2017), and other seismic data sets (Moulik & Ekström, 2016), but some of the methods average over the lowermost few hundred to 1000 km (Lau et al., 2017) and results vary from slightly positively buoyant LLSVP areas to an excess density of 0.5-1.0% in the lowermost 300-400 km.

An intrinsic density excess for pile materials would be mainly linked to the Fe/Mg ratio of the ferromagnesian minerals, whereas the pile viscosity is highly dependent on the mineral assemblage. Bridgmanitic pile material with about 16 mol% $FeAlO_3$ component would agree with the seismologically inferred density excess, and is a likely outcome of BMO crystallization during a period of core-BMO exchange (Trønnes et al., 2019). Transfer of FeO from the BMO to the core and SiO_2 in the opposite direction would suppress the (Fe+Mg)/Si and Fe/Mg ratios in the solidifying BMO, greatly reducing the propoertion of ferropericlase in the crystallizing assemblage. Bridgmanite has a considerably higher viscosity than ferropericlase, and especially post-bridgmanite (Ammann et al., 2010).

Due to its high bulk modulus, the density excess of recycled basaltic material relative to peridotite will decrease with increasing depth through the lower mantle, likely approaching neutral buoyancy in the D" zone when including both intrinsic excess density and thermal effects (Ballmer et al., 2015; Torsvik et al., 2016, and references therein). Thermochemical piles may thus comprise highly viscous and stable lower bridgmanitic layers, maybe 100-300 km thick, overlain by less stable basaltic crust accumulations that can be more easily entrained into rising plumes (Ballmer et al., 2016; Torsvik et al., 2016). Basaltic material is likely to have low viscosity due to the presence of post-bridgmanite with more than 20 mol% $FeSiO_3$ component, even in the upper parts of hot thermochemical piles (e.g., Koelemeijer et al., 2018; Trønnes et al., 2019). This is because $FeSiO_3$ depresses the bridgmanite to post-bridgmanite phase transition to considerably lower pressures than the $FeAlO_3$ component can do. A pile structure with an upper part of less stable recycled oceanic crust may also be supported by the geochemistry of plume-related oceanic islands, recording variable U/Th ratios and U-Pb model ages ranging from 2.7 to 1.5 Ga (Andersen et al., 2015; Torsvik et al., 2016). Geodynamic models also indicate that the accumulation of basaltic material to form stable thermochemical piles may be inhibited under certain conditions (M. Li & McNamara, 2013; Mulyukova et al., 2015; Ballmer et al., 2016), possibly resulting in variable stability in space and time.

It has been shown, both numerically and in laboratory experiments, that a certain excess density is required to avoid extensive entrainment of pile material within mantle plumes (e.g., Davaille et al., 2002; Tackley, 2012; Heyn et al., 2018). A high temperature-dependence of viscosity (Y. Li et al., 2014) or an increase in viscosity due to composition (Davaille et al., 2002; Heyn et al., 2018) can help to increase the amount of LLSVP material that survives ongoing convection. With respect to spatial stability, Conrad et al. (2013) show that the positions of net divergence in plate motion are stably located above the current positions of the LLSVPs, and that these positions have remained stable for at least 250 Myr. Furthermore, reconstructed eruption sites of Large Igneous Provinces (LIPs, Figure 1) and kimberlites have been used to argue that the degree-2 structure of the lowermost mantle has been stable for at least the last 300 Myr, assuming that they are related to plumes rising almost vertically (French & Romanowicz, 2015) from the edges of the LLSVPs where they are generated (Torsvik et al., 2006, 2010; Steinberger & Torsvik, 2012; Torsvik et al., 2016). Although the correlation between projected pile margins and the locations of eruption locations has been questioned (Austermann et al., 2014; Davies et al., 2015), geodynamic models show both plumes rising at the edges and/or the centres of thermochemical piles (e.g., McNamara & Zhong, 2004, 2005; Tan et al., 2011; Steinberger & Torsvik, 2012; M. Li & Zhong, 2017; Dannberg & Gassmöller, 2018; Heyn et al., 2018).

So far, interactions between plumes and pile margins have mostly been investigated with respect to formation of zoned plumes and the behaviour of rheologic and compositional heterogeneities within the plume conduit (e.g., Dannberg & Sobolev, 2015; Jones et al., 2016; Dannberg & Gassmöller, 2018; Farnetani et al., 2018). Yet, these models do not consider the long-term evolution of plume-pile interaction, nor do they investigate the mechanism for how plumes form at the edges of the piles. One idea is that the flow along the CMB, induced by the slabs sinking between the LLSVPs, is forced upwards at the pile edges and thereby results in plumes (Steinberger & Torsvik, 2012; Tan et al., 2011; M. Li & Zhong, 2017; Dannberg & Gassmöller, 2018). However, none of these studies explore in more detail how plumes are generated at the CMB, i.e. how the lower thermal boundary layer becomes thickened sufficently to become unstable and form a plume. M. Li and Zhong (2017) discuss the growth of the thermal boundary layer and conditions for forming instabilities, but do not specifically investigate the influence of a dense thermochemical pile in that process. However, they do show that either decreasing thermal expansivity or increasing conductivity with depth reduces the number of plumes forming from a thermal boundary layer outside dense piles.

Although the use of plate motion history has proven to play a crucial role in focussing mantle upwellings onto specific areas of the CMB (e.g., Davies et al., 2012; M. Li & Zhong, 2017), some plumes are always randomly initiated from the thermal boundary layer, and do not end up in locations close to present day hotspots (French & Romanowicz, 2015). Thus, plate history alone cannot fully explain the distribution of present-day hotspots around the LLSVP margins (French & Romanowicz, 2015). Going back in time, eruption sites of LIPs indicate the persistence of an uneven plume distribution for the last 300 Myr, even though the record of LIPs is most likely incomplete due to subducted oceanic LIPs (Torsvik et al., 2016; Torsvik, 2019). Nevertheless, a concentration of 8 LIPs erupted between 95-155 Ma in the southeastern corner of the African LLSVP (Figure 1) presents an example of plume initiation in close proximity both in space and time (Torsvik et al., 2016; Torsvik, 2019). This proximity is difficult to explain by random plume initiation.

Consequently, a mechanism for plume initiation directly at the pile margin may be better suited to explain the observed correlation between LIPs and the LLSVP margins. This may be especially relevant since the presence of weak post-bridgmanite is likely to aid transforming subducted slabs into a broad and spread-out downwelling of cold material in the lowermost mantle, potentially erasing any "memory" of distinct slabs. In this case, lateral flow along the CMB will be steady and directed almost radially towards the piles (see Figure 1), with only the magnitude of flow varying in time and space. A first step was done by M. Li et al. (2018), who showed that pile motion in response to rising plumes can affect the generation of new thermal instabilities, resulting in an almost periodic behaviour. Yet, in most of their models, plumes rise from the centre of tent-shaped piles that move up and down, and it remains unclear what controls the periodicity of plumes and how plume formation relates to the large-scale mantle flow. In this study, we use 2-D numerical simulations in which we track the formation and motion of plumes, as well as their interaction with dense thermochemical piles, and in particular their effect on the lateral and vertical motion of the pile edge. In contrast to M. Li et al. (2018), our study focuses on the formation of plumes at pile margins and their interaction with lower mantle flow and dense piles, including the changing morphology of these piles. Furthermore, we investigate controls on the periodicity of this process, and discuss how we may use plume observations to develop new constraints on the viscosity structure of the lower mantle and the LLSVPs.

2 Model setup

2.1 Model parameters and initial condition

Our numerical models are run in 2-D spherical geometry using the finite element code ASPECT (Kronbichler et al., 2012; Heister et al., 2017; He et al., 2017; Bangerth et al., 2018, 2019). Conservation equations for mass, energy and momentum are solved using the Boussinesq approximation. Our setup is similar to Heyn et al. (2018), and we choose parameters so that the reference Rayleigh number for the mantle, which describes the vigor of convection and is defined as

$$Ra = \frac{\alpha \rho g \Delta T d^3}{\kappa \eta}, \tag{1}$$

is set to 10^7. Parameters are the thermal expansivity α, the density ρ, the temperature drop across the mantle ΔT, the gravitational acceleration g, the mantle thickness d, the reference viscosity η and the thermal diffusivity κ. We use a quarter of an annulus along the equator as a domain, with a grid that is adaptively refined every 10 time steps based on compositon and viscosity gradients. The effective resolution (lateral x radial) thus varies between about 7 x 11 km and 80 x 90 km. All parameters characterizing the general setup are given in Table 1.

Following Heyn et al. (2018), we impose a constant uniform velocity boundary condition of 1.48 cm/year on the surface to force a single-plate degree-2 flow structure (Figure 2), while all other boundaries are free-slip. However, in order to test the influence of the velocity boundary condition on our results, we also perform tests in which we vary the velocity between 0.74 and 2.96 cm/yr or apply a time-varying periodic plate velocity. For the latter, the velocity is given as

$$v_{\text{Plate}} = v_0 \left(1.2 + \cos\left(\frac{2\pi}{\mathcal{T}_{\text{Plate}}} \cdot (t - t_0) \right) \right), \tag{2}$$

where the reference velocity is $v_0 = 1.25$ cm/year, t is time in years, the start time of the model is $t_0 = 6.5 \cdot 10^9$ years, and the plate velocity period is $\mathcal{T}_{\text{Plate}}$, which is varied between 125 and 1000 Myr. The effective velocity always oscillates between 0.296 and 3.256 cm/yr. This setup ensures that the degree-2 structure is never destroyed and that subduction never ceases completely.

Heat is introduced into the system by basal and internal heating (Table 1). Dense piles are simplified by assuming only bridgmanitic material, and are represented by a compositional field that is advected using the discontinuous Galerkin method (He et al., 2017), which gives similar pile masses and volumes after 4.5 Gyr as the tracer approach used by (Heyn et al., 2018). The density contrast between enriched and regular mantle is defined via the buoyancy ratio

$$B = \frac{\Delta\rho_C}{\alpha\rho\Delta T}, \tag{3}$$

where $\Delta\rho_C$ is the density difference due to composition (see also Table 1).

As in Heyn et al. (2018), viscosity depends on temperature, depth and composition, given by

$$\begin{aligned} \eta(z,T,C) &= \eta_0(z)\eta_{\Delta T}(z,T)\exp\left[C\ln\eta_C\right] \\ &= \eta_0(z)\exp\left[\frac{E_\eta(z)}{T^* + T_\eta(z)} - \frac{E_\eta(z)}{1+T_\eta(z)} + C\ln\eta_C\right] \end{aligned} \tag{4}$$

where the non-dimensionalised temperature T^* is restricted to values between 0 and 1. Non-dimensionalisation is achieved using the surface and the CMB temperatures as references for $T^* = 0$ and $T^* = 1$, respectively. The depth-dependence is implemented as stepwise adjustments of the viscosity prefactor η_0, the non-dimensional activation energy E_η and the non-dimensional temperature offset T_η (see Table 2). C is the composition value between 0 and 1, and η_C is the intrinsic viscosity contrast assigned to a composition value of $C = 1$. The thermal viscosity contrast $\eta_{\Delta T}$ describes the maximum potential viscosity variations due to temperature in the lower mantle and is varied in the range 2.3 to 55000, while we vary η_C between 1 and 100. In addition, we conducted a few tests with isochemical models to investigate the importance of thermochemical piles for plume generation (see Figure 2d).

All models are initiated from the same reference state of a fully-developed system with an existing degree-2 structure (see Figures 2a and 2b). This is obtained by running a model with the reference values of $B = 0.8$, $\eta_{\Delta T} = 330$ and $\eta_C = 10$ for 6.5 Gyr (corresponding to t_0 in equation (2)) starting at $t = 0$ with a 125 km thick dense basal layer (as described in Heyn et al. (2018)). This setup results in a broad thermal downwelling that accumulates slab material in the lowermost mantle (Figure 2b), comparable to what is observed by seismic tomography (Figure 1), and a pile with a volume equal to about 1.75 % of the mantle at $t = t_0$. Approximately 77% of the original material remains in the pile of the reference state. Although such a setup means that models can take some time to adjust to changes in parameters (especially a change in the velocity boundary condition as shown below), it enables us to directly compare results and analyse dependences on various parameters without having to worry about variations in pile mass retained after 4.5 Gyr of convection (see Heyn et al. (2018) for more details about how much mass changes with $\eta_{\Delta T}$ and η_C). Moreover, it allows us to estimate the time that the system takes to adjust to new conditions, such as changes in plate velocity during a supercontinent cycle (e.g., Matthews et al., 2016). To overcome the limitation of adjustment time and to get better constraints on plume properties, we run the models for 2.5 Gyr in order to examine several plumes rising from the same location.

2.2 Detection of plumes

We detect plumes by calculating profiles of temperature and radial velocity versus longitude at a specific radius and tracking their maxima. An example of such a profile for temperature is shown in Figure 2c. The innermost white circle segment across the temperature field (Figure 2b) indicates the profile radius of 4000 km (519 km above the CMB), along which the temperature shown in Figure 2c is projected. As can be seen in Figure 2a, a radius of 4000 km is just above the top of the thermochemical pile for this set of parameters. A profile closer to the CMB would partly cut through the pile, which makes the detection and interpretation of plumes significantly less reliable. However, actual pile thickness varies with parameters, especially the density contrast (e.g., McNamara & Zhong, 2004; Heyn et al., 2018). Consequently, we choose radii of 4000 km, 4200 km or 4500 km (corresponding to 519 km, 719 km and 1019 km above the CMB, respectively) for our analysis, depending on the thickness of the pile. In most cases, a radius of 4200 km is used. The excess temperature (or radial velocity) for each time step is then obtained by calculating the difference between the maximum and the highest local minimum next to this maximum (as indicated by the vertical red line in Figure 2c). The width of the plume is defined as the width of the peak taken at the value of the minimum used to obtain the amplitude (see red horizontal line in Figure 2c).

We are mostly interested in plumes around the pile edges, and in fact all plumes in our models are either generated there or on the CMB outside the piles and then pushed towards the pile edge. Thus, in this study, we only track the maxima of temperature and radial velocity within a range of 10 degrees from the edge outside of the pile and 15 degrees from the edge towards the pile centre. This choice usually avoids complexities in plume detection associated with the general upwelling above the pile centre. The maxima are tracked over time from their appearance (either marked by the beginning of the thermal instability or by the motion of the pile into the respective lateral range around the pile edge) until they disappear (plume fades or moves out of range towards the pile centre). For each plume, we calculate the maximum excess temperature and excess velocity, which usually marks the passing of the plume head through the respective radius. To even out natural variations in plume properties that are not related to changes in parameters, we calculate averages of plume characteristics such as the plume periodicity.

3 Mechanism of plume generation

As pointed out by M. Li et al. (2018), a thermochemical pile can respond to a rising plume by being uplifted. However, most of their models feature plumes rising from the centre of tent-shaped piles, with only a few of them showing plumes rising at the pile margins. In contrast, our models predict plumes rising solely from pile margins, with a more localized interaction between plume and pile. Figure 3 shows the temporal evolution of this interplay as a zoom-in on the pile edge. As can be seen in the temperature field, the plume that is visible in the first stage (Figure 3a) is slowly pushed further towards the centre of the pile by the general flow along the CMB (Figure 3b). During this process, hot pile material is lifted up by the plume via viscous drag (later named plume pull), which increases the local pile thickness and reduces the CMB area that is covered by the pile (indicated by pile outlines), resulting in a steepening of the pile margin. When the plume moves further towards the pile centre (Figure 3c), the position of the maximum thickness moves along with the upward pull of the plume. When the plume is pushed onto the top of the pile and loses its connection to the lower thermal boundary layer, it weakens, thereby reducing the plume pull. Moreover, the plume heat extracted from the pile causes the top of the pile to cool down and increase its density. As a consequence, the pile top becomes gravitationally unstable, eventually resulting in a collapse of the thickened pile edge (Figure 3d). Subsequently, the pile material spreads along the CMB, pushing the hot thermal boundary layer next to it against the dominant flow direction resulting from subduction (Figure 3e). The subsequent local thickening of the hot thermal boundary layer outside the thermochemical pile marks the beginning of a new plume (Figure 3f), which then repeats the process.

The motion of the pile edge, and thus the cyclicity of plume generation can be seen in more detail in Figure 4 and the Movie S1. The thickness at 5 degrees into the pile shows a periodicity of about 350-400 Myr (Figure 4a), reflecting the plumes recorded at 719 km above the CMB about 70-120 Myr later (Figure 4c). The same periodicity, delayed by approximately 30-40 Myr, is also visible in the lateral motion of the pile edge (Figure 4b). This delay shows that the pile collapse starts within the pile and is not initiated by a motion of the pile edge itself. Notice that the amplitudes of pile motion and thickness variations are not constant, but reflect amongst other aspects the strength of the individual plumes. Further into the pile, the variations in thickness become less representative of the plume cycle, with the similarity almost lost by 15 degrees away from the edge. The thickness close to the pile centre (Figure 4d) does not resemble the plume cycle, indicating that pile thickening and collapse during the plume cycle are only localized within about 5-10 degrees from the pile edge. The rapid changes in pile thickness observed for positions close to the pile centre or more than about 10 degrees from the pile edge are related to the fact that the pile top is ususally rather jagged due to pile filaments advected with and folded by mantle flow (see Figure 2a and Movie S1).

The results shown in this section are obtained for the reference parameters $B = 0.8$, $\eta_{\Delta T} = 330$ and $\eta_C = 10$, but we find no major change in behaviour when altering any of the three parameters B, $\eta_{\Delta T}$ or η_C (Figure 4e-g). Decreasing or increasing the bouyancy ratio B affects the temporal stability of the pile (e.g., Heyn et al., 2018) and can add complexities in case the low density results in unstable piles. Moreover, increased density results in flatter piles, and thus also reduces pile edge motion and thickness variations (see Figure 4g). Increasing the compositional viscosity contrast η_C also reduces pile motion (Figure 4e), with both lateral motions of the pile edge and thickness variations diminished. Even for cases with $\eta_C = 2000$ or $\eta_C = 1e4$, the pile edge motion is visible, although resulting plumes are weaker since the lateral motion of pile material provides less additional thickening of the TBL. In contrast, increasing $\eta_{\Delta T}$ has little effect and only slightly increases pile motion (Figure 4f). However, the mechanism for plume-pile interaction and the correlation between the plume cycle and pile motion are not affected by the choice of these parameters. Test runs for which the surface velocity boundary condition has been replaced by a free-slip boundary show a similar behaviour of plume initation due to a collapsing and expanding pile, but the regime changes shortly after subduction because the lateral flow along the CMB stops. In this case, plumes are no longer pushed towards the pile interior, and plumes start forming randomly from a growing thermal boundary layer.

4 Plume periodicity

The plume period observed in the models above evolves naturally from the given set of parameters. Yet, the actual period with which plumes form at the pile edge varies significantly for different choices of parameters. While most plumes in our models form at pile margins due to pile collapse, some models exhibit plumes that form at a distance from the pile without responding to pile edge motion. In the following section, we will explore the controls on the "natural" period of plume formation, and how it can be overprinted by the influence of mantle convection.

4.1 The two "natural" plume periods

4.1.1 Thermal boundary layer period $\mathcal{T}_{\mathrm{TBL}}$

Plumes in a basally-heated convection model without a dense component form as thermal instabilities of the lower thermal boundary layer (TBL). When the TBL grows in thickness due to heat conduction, it can reach a thickness for which the local Rayleigh number Ra_l is above a critical value, and an instability forms (Howard, 1966). How often such instabilities form, i.e. the "natural" plume period of the lower TBL ($\mathcal{T}_{\mathrm{TBL}}$), is determined by the parameters that affect Ra_l. Due to their respective uncertainties within Earth, the most important parameters are the thermal expansivity α, the thermal diffusivity κ and the viscosity η (M. Li & Zhong, 2017), of which the viscosity is the most poorly constrained (Tackley, 2012). A lower value of Ra_l, for example due to higher viscosity or thermal diffusivity or a lower thermal expansivity, reduces the number of plumes forming in time (M. Li & Zhong, 2017). Thus, $\mathcal{T}_{\mathrm{TBL}}$ is fundamental to Ra_l and independent of the pile properties.

The plume initiation process outlined above is restricted to the TBL outside the thermochemical pile areas, because conductive growth of a TBL on top of a thermochemical pile is slow, and because this thin layer is repeatedly emptied by plumes being pushed on top of piles and by the broad-scale upwelling above piles. Since the TBL at the CMB grows everywhere, with additional thickening caused by lateral flow along the CMB, plume generation is not necessarily limited to the pile margins. Thus, depending on the plate velocity and thermal viscosity contrast, we might expect to see a certain percentage of plumes forming (far) away from the pile (M. Li & Zhong, 2017). In fact, some of our models, especially those with reduced plate velocity and therefore reduced lateral TBL flow, show plumes forming away from the pile edge as discussed below. M. Li and Zhong (2017) have shown that a reduction of the local Rayleigh number Ra_l reduces the number of plumes forming (far) away from the pile, yet neither thermal expansivity α nor diffusivity κ are changed within our models, and our viscosity law (equation (4)) does not change the viscosity of the hot lower TBL significantly with $\eta_{\Delta T}$. Viscosity above the TBL is affected by $\eta_{\Delta T}$, but does not impact plume initiation. Consqeuently, Ra_l within the TBL remains almost the same for all models and minor variations in Ra_l alone can only explain small changes in the number of initiated plumes in our models. Moreover, plumes forming at random locations and times from a lower TBL are not necessarily expected to cause a periodic signal at the pile edges, and tests with isochemical models with the same parameters as our reference case (but without thermochemical piles) indicate that plumes will form closer to the domain edge when no piles are present (see Figure 2d). Such plumes form less frequently and more aperiodically than we find for plumes rising from the edges of our thermochemical piles.

4.1.2 Slab-pile period $\mathcal{T}_{\mathrm{Pile}}$

As pointed out above, plumes at the pile margin can be initiated by a periodic pile collapse with period $\mathcal{T}_{\mathrm{Pile}}$. In order for the pile collapse to trigger a plume, the TBL has to be close enough to its critical thickness such that the spreading pile material provides sufficient additional local thickening to form an instability. The pile collapse is to first order independent of Ra_l, since it responds to how fast plumes lose their ability to support a thicker pile. This occurs when the upward-directed viscous drag of the plume becomes smaller than the downward-directed gravitational force on the uplifted dense pile. In contrast, Ra_l only affects the initial plume strength, reflecting how often and how effectively plumes reduce the TBL thickness (see also section 5), and thus determines how much pile material can be pulled upwards during plume initiation. However, the plume period $\mathcal{T}_{\mathrm{Pile}}$ depends on the lateral motion of the plume, which is controlled by the plate velocity (see next section) and the sinking velocity of slabs in the lower mantle (controlled by $\eta_{\Delta T}$). Figure 5a shows the period of plumes versus the compositional viscosity contrast η_C for all tested values of the temperature-dependence of viscosity $\eta_{\Delta T}$. As can be seen, each value of $\eta_{\Delta T}$ has its own characteristic period with considerably larger differences than we would expect from variations in the local Rayleigh number, while intrinsic pile viscosity contrast η_C (Figure 5a) or the excess density of the pile (B) play minor roles (Figure 5b).

The reason that none of the actual pile properties (B or η_C) affect the plume period relates to the connection between the plume and the TBL. As long as growing plumes are located directly above the pile margin and are fed by a continuous supply of hot TBL material, their lower parts are able to maintain high temperatures, while the plume buoyancy provides upward pull on the pile margin. When the lateral flow (mantle wind) pushes the plume roots towards the pile centre, the supply of hot TBL material declines and plumes begin to weaken at their base since the pile material itself is too dense to provide sufficient influx. As a consequence, and due to the fact that the plume continues to move above the pile, the thickened pile edge contacts directly with the colder ambient mantle and cools down more efficiently by conduction. Pile collapse is then triggered by the combination of reduced plume pull ("plume weakening"), the lateral motion of the plume, and pile cooling. Therefore, the strength of the mantle wind close to the CMB, which is the same as the velocity of the slab material spreading along the CMB (v_{CMB}), controls the period of pile collapse. This spreading velocity is related to the rate at which cold material is supplied to the lowermost mantle and thus to the sinking velocity of slabs in the lower mantle. Since increasing $\eta_{\Delta T}$ increases the effective viscosity of the slab in our models, both sinking and CMB spreading velocity are reduced and plumes are generated less frequently. The plate velocity has an even stronger effect on slab sinking velocity, as will be discussed in the next section, but the results shown in Figure 5a and 5b are obtained for the same plate velocity. Thus, v_{CMB} determines the plume period of the slab-pile system $\mathcal{T}_{\mathrm{Pile}}$.

4.1.3 Observed period

The effective period of plume initiation at the CMB is a combination of the two processes described above, i.e. thermal instabilities rising randomly from the lower TBL and pile collapse. If the "natural" plume period of the lower TBL is longer than the period given by the slab-pile system, i.e. $\mathcal{T}_{\mathrm{TBL}} > \mathcal{T}_{\mathrm{Pile}}$, plumes will be predominantely initiated near an outwards extending pile edge associated with pile collapse. Otherwise ($\mathcal{T}_{\mathrm{TBL}} < \mathcal{T}_{\mathrm{Pile}}$), most of the plumes will be generated away from the pile (see Figure 5d), and subsequently pushed towards the pile where they may interact and merge with other plumes.

Independent of plume initiation away from the pile, the pile collapse caused by fading of the previous plume creates a thermal instability, which starts to rise at the pile margin. In most cases, e.g. for low plate velocities or some metastable piles (Heyn et al., 2018), plumes forming outside the pile and at the pile margin will simultaneously coexist only for a short while before they merge. A similar process of plume merging can be observed if the temporal spacing between plumes gets small, e.g. for some models with large plate velocities. In these cases, our plume detection algorithm may identify them as a single plume with pulsating flux, making the determination of plume properties (e.g. period, lifetime) more difficult. For this reason, we calculated the standard deviation of our averages and excluded data points with a standard deviation higher than 50% of the mean value (see e.g., missing points for $B = 0.6$ in Figure 5b and the lowest velocity in 5c). Most of the standard deviations are in the range of 10-20% of the mean value.

4.2 The effect of plate velocity on plume period

4.2.1 Constant plate velocity

The observed plume period is furthermore altered by the plate velocity (Figure 5c), which affects the slab sinking rate in the lower mantle and the lateral TBL flow (mantle wind). A higher plate velocity therefore results in more slab material at the CMB and more frequent plume generation at the pile margin. A reduced plate velocity has the opposite effect, creating less frequent plumes, most of which initiate away from the pile (Figure 5d). In both cases, the lower mantle reacts rapidly (within a few tens of Myr) to the modified plate velocity, although the change in plume excess temperature and plume period gets more pronounced after aproximately 50-100 Myr. Changes in plate velocity have a stronger effect on slab sinking velocity, and thus plume period, than changes in the thermal viscosity contrast $\eta_{\Delta T}$. The excess temperature of plumes in models with a high plate velocity is significantly smaller since the lower TBL has less time to heat up and grow between plumes.

4.2.2 Periodic plate velocity

More interesting than the effect of a constant velocity is the impact of time-variable plate motion. To test this, we have prescribed velocity v_{Plate} as cosine function in time (equation (2)) with different periods, ranging from $\mathcal{T}_{\mathrm{Plate}} = 125$ Myr to $\mathcal{T}_{\mathrm{Plate}} = 1$ Gyr.

This simulates changes in plate velocities as they may occur during a supercontinent cycle (Matthews et al., 2016), although neglecting lateral motions of the subduction zones (as discussed later). As can be seen in Figure 6, the plume cycle can adjust to $\mathcal{T}_{\mathrm{Plate}}$ within a certain resonance range around $\mathcal{T}_{\mathrm{Pile}}$, i.e. values of $\mathcal{T}_{\mathrm{Plate}}$ that are close enough to $\mathcal{T}_{\mathrm{Pile}}$. While an imposed plate velocity with a period of 250 Myr (as may be expected for Earth's supercontinents) for our model with $B = 0.8$, $\eta_{\Delta T} = 330$ and $\eta_C = 10$ forces the plume cycle to follow a similar period after an adjustment time of about 1 Gyr (Figure 6a-d), a higher $\mathcal{T}_{\mathrm{Plate}}$ of 125 Myr cannot be enforced for the plume cycle (Figure 6e-h). The reason for this can be seen from the motion of the pile edges (Figure 6c and 6g) and the variation of pile thickness at 5 degrees from the pile edge (Figure 6d and 6h). While the pile edge motion in both cases reflects the plate velocity cycle and thus the strength of lateral TBL flow (Figure 6c and 6g), the thickness of the pile as the driving mechanism for plume generation only reflects the plume cycle (compare Figure 6b and 6f with 6d and 6h). In fact, for plate velocity periods below the lower limit of a certain resonance range, in this case between 250 Myr and 125 Myr, plume motion and the pile react as if the velocity were constant (compare Figure 6h and Figure 4a). In these cases, the lateral motion of the pile edge is the superposition of the motion caused by the variable plate velocity and pile collapse (Figure 6g).

A similar observation can be made for very long cycles of 1 Gyr (not shown), although more plumes start away from the pile during times of low plate velocity and the plume cycle becomes aperiodic to a certain extent. Thus, plate velocity cycles are only reflected in plume periods if they are within the resonance range of the slab-pile system, which depends on $\mathcal{T}_{\mathrm{Pile}}$. Within that range, the system adjusts such that every plate cycle corresponds to a plume ($\mathcal{T}_{\mathrm{Pile}} = \mathcal{T}_{\mathrm{Plate}}$). For shorter plate velocity periods, the observed plume period $\mathcal{T}_{\mathrm{Pile}}$ reflects the constant average of velocity. For longer plate periods, the observed plume period becomes more chaotic due to plumes forming far away from the pile. Yet, the push from lateral TBL flow on the pile margin still reflects plate velocity cycles, even for long or short periods. As a consequence, the lateral motion of the pile edge in these cases reflects both $\mathcal{T}_{\mathrm{Plate}}$ and the plume cycle as a superposition of the two periods, while the pile thickness only captures the plume cycle. In case of our reference model, the reference period of the slab-pile system $\mathcal{T}_{\mathrm{Pile}}$ is about 370 Myr, and the lower and upper limits of the resonance range are somewhere between 125 and 250 Myr and between 500 and 1000 Myr, respectively, since neither 125 Myr nor 1 Gyr periods can be stimulated while plume periods at 250 and 500 Myr can be. A higher value of $\eta_{\Delta T}$, or a lower average velocity, should move the resonance range towards longer plume periods (Figure 5).

5 Plume buoyancy flux and lifetime

A change in plume period is reflected in other properties of the plumes, for example their excess temperature. While a system with $\mathcal{T}_{\mathrm{TBL}} < \mathcal{T}_{\mathrm{Pile}}$ is characterised by a large number of plumes forming independently of pile collapse, we expect the case $\mathcal{T}_{\mathrm{TBL}} > \mathcal{T}_{\mathrm{Pile}}$ to be reflected in lower plume strength as the TBL has insufficient time to grow thick enough to form instabilities naturally. Figure 7a shows the excess temperature of detected plumes for a model with the same parameters as our reference model, except that the velocity has been increased to 2.96 cm/year. The radius at which these temperatures are taken is lower (519 km above the CMB instead of 719 km), since weaker plumes are more difficult to detect and fade away more easily. This precludes a direct comparison to Figure 4c, but the first plume in Figure 7a has not been affected significantly by the increased velocity because it falls within the adjustment time of the model after modifying the velocity. As a consequence, it can be used as a reference to which later plumes can be compared.

In order to compare plumes between the different models, we calculate the averages of buoyancy flux (Figure 7b and 7d) and lifetime (Figure 7c) for all plumes detected during the simulation time. Our definition of lifetime reflects the time that each plume stays within the given lateral distance range around the pile edge. The buoyancy flux, neglecting small amounts of dense material entrained in the plume, is calculated according to the formula $B = \int v_{\mathrm{r}} \rho \alpha \Delta T_{\mathrm{P}} dS$ with the plume excess temperature ΔT_{P} and radial velocity v_{r} (e.g., Dannberg & Sobolev, 2015; Farnetani et al., 2018), assuming a rotational symmetry around the central plume axis to obtain 3-D buoyancy fluxes. Buoyancy flux is a good measure of plume strength since it combines both excess temperature and radial (vertical) velocity and integrates over the width of the plume (Dannberg & Sobolev, 2015; Farnetani et al., 2018). However, determinations of lifetime and buoyancy flux get more complicated for plumes that merge together. Although plume bouyancy fluxes depend on the viscosity and may be strongly time-dependent, our estimated values are in a similar range as those obtained by analysis of hotspot swells (King & Adam, 2014). Note, however, that our definition marks the maximum buoyancy flux for each plume, which usually corresponds to the plume head.

5.1 Effect of plate velocity

As can be expected, the lifetime of plumes decreases with increasing plate velocity (see Figure 7c). The reason is that plumes are more easily pushed out of the range around the pile margin (and thus out of the area where we track them), but they also lose their connection to the hot TBL and therefore fade away more quickly. Moreover, plumes created under high plate velocities are weaker (low buoyancy flux at their onset, Figure 7b), because the thermal boundary layer has less time to grow and plumes contain less material. Thus forcing plumes to adopt to a shorter period than the "natural" period results in overall weaker plumes that are less enduring.

A similar observation can also be made for periodic plate velocities. The shortest plate velocity period $\mathcal{T}_{\text{Plate}}$ within the resonance range forces the highest number of plumes, and thus the weakest plumes (compare Figure 6 second row panels), although the difference in plume excess temperature is only about 200 K. Shorter or longer plate velocity periods result in less frequent, but stronger plumes since the TBL has more time to grow. Plume lifetimes are more complicated to interpret, since the mantle wind v_{CMB} changes significantly with time. Within the resonance range, lifetimes increase with longer $\mathcal{T}_{\text{Plate}}$ as maxima in v_{CMB} are less frequent. Outside the resonance range, lifetimes either adjust to the constant average velocity ($\mathcal{T}_{\text{Plate}}$ < resonance range), or become more chaotic and less reliable due to plume formation away from the pile ($\mathcal{T}_{\text{Plate}}$ > resonance range).

5.2 Effect of viscosity and pile density

In contrast to changing the plate velocity, a change in the temperature dependence $\eta_{\Delta T}$ alters the plume period (Figure 5a), but the effect on plume lifetime or buoyancy flux is negligible (see different colors in Figures 7b-d). A higher value of $\eta_{\Delta T}$ slightly reduces the lateral CMB flow v_{CMB}, which decreases lateral plume motion and TBL thickening due to TBL flow. Yet, the system stays relatively close to the natural plume period of the lower TBL ($\mathcal{T}_{\text{TBL}} \approx \mathcal{T}_{\text{Pile}}$), causing only minor variations in plume strength. Since plumes stay longer around the pile margin, they can increase pile edge thickness more, which also increases the lateral mobility of the pile edge during plume cycles (compare Figures 4b and 4f). Thus, during a pile collapse, the pile margin moves faster and further, locally increasing the TBL thickness within a short time. Consequently, plumes, triggered either by the pile collapse or initiated away from the pile, abruptly enter or leave the range around the pile margin, reducing their detected lifetimes around the pile margin.

Increasing the density or the compositional viscosity contrast tends to decrease plume buoyancy flux (compare Figure 7d). This reflects two aspects: 1) the effect of reduced lateral and vertical motion of the pile edge, resulting in a slightly smaller thermal instability; and 2) a reduction of plume ascent velocity related to the higher density or viscosity of entrained material, increasing the average density or viscosity of the rising plume. Yet, in contrast to the effect of plate velocity, a reduction in plume flux is not related to a significant decrease in the excess temperature of plumes. Consqeuently, the reduction in plume buoyancy flux is more or less independent of the temperature-dependence of the viscosity.

In summary, both bouyancy flux and lifetime (or residence time around the pile edge) of plumes are mostly affected by plate velocity, while other parameters play minor roles. In particular, if plate velocity forces plumes at considerably shorter period than $\mathcal{T}_{\mathrm{TBL}}$ (the natural period of the lower thermal boundary layer), this is reflected in significant reduction in buoyancy flux and lifetime. Consequently, buoyancy flux and the number of plumes away from the pile give indications how close the system is to $\mathcal{T}_{\mathrm{TBL}}$. A large number of plumes forming (far) away from the pile edges indicate $\mathcal{T}_{\mathrm{TBL}} < \mathcal{T}_{\mathrm{Pile}}$, while a low buoyancy flux means $\mathcal{T}_{\mathrm{TBL}} > \mathcal{T}_{\mathrm{Pile}}$.

6 Discussion

As shown above, plumes are initiated at the CMB when the thickness of the lower thermal boundary layer reaches a critical value, which is defined by the local Rayleigh number Ra_l (Deschamps & Tackley, 2008; M. Li & Zhong, 2017). The boundary layer grows conductively over time, with additional thickening due slab-induced lateral flow along the CMB, causing spontaneous thermal instabilities. This plume generation mechanism is independent of the presence or properties of a thermochemical pile and does not predict where the plume will be initiated. Plume generation is generally suppressed by a decrease in thermal expansivity or an increase in conductivity towards the CMB, which are both expected for Earth (Tackley, 2012) and would reduce Ra_l (M. Li & Zhong, 2017).

A decrease in viscosity, e.g. due to the presence of weak post-bridgmanite (Ammann et al., 2010; Koelemeijer et al., 2018) as discussed below, may offset this effect.

Yet, a pile may trigger "early" plume formation by providing a localized thickening of the TBL due to an expanding pile margin associated with a pile collapse, with "early" being relative to the time frame set by conductive growth of the TBL, $\mathcal{T}_{\mathrm{TBL}}$ (compare Figure 3). This "early" plume initiation always results in plumes forming at the pile margin and, depending on parameters such as viscosity or plate velocity, may be the dominant mechanism.

6.1 Model limitations

In our 2-D models, both "regular" and "early" plumes mentioned above may eventually end up rising at the same location, the pile margin, resulting in a periodic behaviour of plume generation. In 3-D, however, this does not necessarily hold true any longer. We cannot expect "early" plumes to rise at exactly the same location along the pile margin since a collapsing pile edge would increase the thickness of the lower TBL in an area around it, and plumes would draw in material from within a certain radius. These 3-D effects may cause plume initiation to be less periodic in global models as plumes may rise from several different locations around the piles. On the other hand, 3-D plumes may be stronger since they can draw material from a radius and focus it into a columnar upwelling (instead of rising sheets as in 2-D models), locally resulting in a higher positive bouyancy flux. Therefore, they may rise faster than they do in our 2-D models, which tend to overestimate plume rise times. Plume rise velocities may also be affected by depth-dependent values for viscosity, thermal diffusivity and thermal expansivity throughout the entire mantle range. Due to these simplifications in our model setup, we cannot investigate the fate of plumes more than a few hundred km above the piles. However, since we are only interested in plume initiation, details of plume rise times are not relevant for the purpose of this study, but should be addressed in future work.

Apart from being 2-D, our models are simplified with respect to subduction processes. As we have no weakening due to yield stress, plates and subduction zones are not forming self-consistently, but are forced by an imposed velocity boundary condition. Furthermore, our models feature neither phase transitions in the mantle transition zone (although we do impose a viscosity jump at 410 km and 660 km) potentially causing slab stagnation, nor subduction zone retreat or advance. As a consequence, we obtain a stable degree-2 convection pattern and a coherent broad downwelling into the lowermost mantle, where it forms a long-wavelength thermal structure (Figure 2b) comparable to what is shown in seismic tomography (see Figure 1). While these simplifications allow us to have more direct control over the lateral velocities within the lower TBL, we do not expect them to have a significant impact on plume initiation dynamics as this process is localized in the lowermost mantle and is not affected by the details of subduction dynamics in the upper mantle. The only way that slabs play a significant role for plume-pile dynamics is via their impact on the lateral TBL flow along the CMB (v_{CMB}), which may be strongly dependent on 3-D effects. The effect of changes in subduction velocity are simulated by modifying the imposed velocity boundary condition, while changes in TBL flow direction would require a 3-D geometry.

The viscosity structure of the lowermost mantle might be further modified by the presence of weak post-bridgmanite (or post-perovskite) (Ammann et al., 2010), although it is not clear whether this phase is present only in cold slabs (Torsvik et al., 2016) or also in hotter areas of the CMB as indicated by Koelemeijer et al. (2018). In the first case, the reduced viscosity of the slab decreases the viscosity contrast between cold material and ambient mantle. This may result in a similar lowermost mantle viscosity structure to what we obtain for small values of $\eta_{\Delta T}$, where piles can be more viscous than slabs. As a consequence, we would expect a comparable behaviour of the plume cycle, i.e. a decrease in plume period and more plumes starting at a distance from the pile edge, in agreement with an increased local Rayleigh number Ra_l (M. Li & Zhong, 2017). In contrast, if weak post-bridgmanite is present (almost) everywhere, except for the hottest part of the lower TBL, both slab and pile viscosity would be reduced. Since the viscosity contrast between pile and slab would be maintained and the TBL's local Rayleigh number is not altered, we would expect a similar behaviour as in our models, although potentially with a slightly shorter plume period due to a general decrease in viscosity. However, the influence of post-bridgmanite may be more complex than our speculation, and further work would be required to understand the detailed impact of weak post-bridgmanite on plume generation.

Finally, our models simplify the potential composite pile structure, and only consider the relatively stable (bridgmanitic) base layer (Ballmer et al., 2016; Trønnes et al., 2019). Inclusion of recycled oceanic crust would require us to add further complexities to the model, both in the upper and the lower mantle. On the other hand, basaltic material on top of the LLSVPs is expected to have very minor density excess, and thus may play a rather passive role in the initiation of plumes, as long as it does not prohibit interaction between the dense basal layer of piles and the rising flow of plumes. Since it seems unlikely that the (potentially low-viscosity) basaltic material completely covers the LLSVP margins, where it would be easily eroded by rising plumes, we would expect that our proposed plume initation mechanism is also applicable to composite pile structures.

6.2 Comparison to other geodynamic models

As mentioned before, M. Li et al. (2018) also show a vertical motion of piles in response to plume initiation, featuring a quasi-periodic behaviour of plume initiation and related pulses in CMB heat flux. However, they do not investigate the controls on this periodicity, e.g. how the plume period relates to large-scale mantle flow and pile dynamics. Moreover, piles in their models are mostly tent-shaped, with plumes rising at the pile centre, and the whole pile moves up and down. In contrast, our models feature plumes rising predominantly at the pile edges, similar to what as been observed for Earth, while plumes fade quickly as soon as they are pushed on top the thermochemical piles. This difference in behaviour may be explained by the geometry (cartesian in M. Li et al. (2018) and spherial in this study), and the difference in lowermost-mantle structure. While we model a degree-2 structure, M. Li et al. (2018) have approximately a degree-5 pattern. Their models thus have much stronger TBL flow, comparable to our cases with increased velocity, and therefore more compressed piles. In this case, small thermal instabilities may form at the pile margins, but are rapidly pushed towards the pile centre (M. Li et al., 2018). This could also explains why M. Li et al. (2018) report a vertical motion of the whole pile structure, while this plume-related motion is locally confined to the edges in our models.

Apart from the collapse of the pile edge, the presence of a physical barrier, i.e. the steep pile margin, may play a role in initiation of plumes. As has been previously suggested, lateral flow of hot TBL material along the core-mantle boundary is forced upwards along a (stationary) pile margin, potentially resulting in plumes (Steinberger & Torsvik, 2012; Torsvik et al., 2016; Dannberg & Gassmöller, 2018). Although we cannot rule out the effects of such a barrier on our flow field, a barrier does not provide an explanation for the dynamic behaviour of our models: (1) As TBL flow for a time-invariant plate velocity is constant and the supply of plume material at the pile margin is uniform, the thickness of the TBL has usually not reached its critical thickness for instabilities to form. Therefore, we would not expect plume initiation at a stable physical barrier to be periodic; (2) As can be seen in Figure 4, each plume initiation starts with a pile collapse and subsequent lateral motion of the pile edge, which provides additional thickening of the lower TBL and can explain the periodicity. As a consequence, our results indicate the predominant impact of local pile edge collapse on plume initiation.

Finally, our observation that plume period increases with thermal viscosity contrast $\eta_{\Delta T}$ (Figure 5a) may explain why a stronger temperature-dependence increases the temporal stability of dense thermochemical piles (e.g., McNamara & Zhong, 2004; Y. Li et al., 2014; Heyn et al., 2018). While plumes in our models become less frequent with increasing $\eta_{\Delta T}$, their buoyancy flux, and thus their potential to entrain dense pile material, remains almost constant (Figures 7b and 7d). In this case, the effective amount of pile material per plume is controlled by the pile density B and the compositional viscosity contrast η_C (Davaille et al., 2002; McNamara & Zhong, 2004; Y. Li et al., 2014; Heyn et al., 2018). Thus, for constant pile properties, longer plume periods, a consqeuence of increased temperature-dependence of viscosity, result in less entrainment over time (Heyn et al., 2018).

6.3 Implications for Earth

Values of pile densities and compositional viscosity contrasts (Table 1) used in our models are within the range typically applied for primordial material in geodynamic studies (e.g., McNamara & Zhong, 2004; Y. Li et al., 2014; Heyn et al., 2018). Mineralogical data supports both increased density and viscosity for bridgmanitic piles, indicating that the viscosity increase may even be greater than set in this work (Trønnes et al., 2019). Yet, the mechanism of plume initation by pile collapse is not directly dependent on pile properties, and thus would not be altered by slightly higher pile viscosities or the incorporation of recycled oceanic crust as an (upper) part of the pile (Ballmer et al., 2016; Torsvik et al., 2016; Trønnes et al., 2019).

Although our models cannot investigate spatial stability of thermochemical piles, we have shown that pile edges can move within a certain range in response to interactions between pile and plumes. This motion is determined by the viscosity of the pile itself (or more precisely the viscosity contrast between pile and ambient mantle) and the lateral TBL flow, which is controlled by the subduction velocity and the temperature-dependence of viscosity. The general pile thickness is in balance with the average strength of the TBL flow, such that the forces of lateral flow (directed towards the pile centre) and gravitational forces within the pile interior, which tend to spread the dense material away from the pile centre, have the same magnitude. While the local pile thickness within about 5 degrees ($\sim 300\,\mathrm{km}$) of the pile margin varies in response to rising plumes, the thickness close to the pile centre does not. Consequently, we can assume that the plume-induced lateral motion of the pile material will not result in significant lateral motion of the pile itself. Thus, as long as the distribution of lateral TBL flow around the pile does not change significantly, we do not expect the pile to move. Consequently, the plume cyle and its associated pile edge motion can explain a scattering of (reconstructed) plume positions within a few degrees around the margin observed today (e.g., Torsvik et al., 2016; Torsvik, 2019) without contradicting the stability of a degree-2 structure. Moreover, the mechanism of plume initiation by a local pile edge collapse would predict that the different margins of the LLSVPs may be at very different stages of the plume cycle, thus giving an alternative to plate history as an explanation (Davies et al., 2012; M. Li & Zhong, 2017) for the distributions of plumes around the LLSVP margins (French & Romanowicz, 2015).

Even though our models predict a periodic generation of plumes, no such cyclicity for plumes has yet been observed in Earth. This may partially be explained by the limited observations of plumes and LIPs that are available for the last 300 Myr (Figure 1), with an unknown number of LIPs lost due subduction of oceanic crust (e.g., Torsvik et al., 2016; Torsvik, 2019), and the poor accuracy of plate reconstructions going back more than a few hundred million years (see e.g., Matthews et al., 2016; Torsvik, 2019). Although several LIPs erupted sequentially during the 155-95 Ma period around the south-eastern corner of the African LLSVP (Torsvik et al., 2016; Torsvik, 2019), their lateral spread and close proximity in time do not provide constraints on plume periodicity in Earth. Based on currently available data, it is therefore difficult to infer potential plume periodicity of 300-500 Myr as observed in our 2-D models. A further explanation for the absence of a clear plume periodicity might be given by the subduction velocity and the configuration of plates, which are both very simplified in our models. As we showed with periodic plate velocities or increased/ decreased plate speeds, subduction velocities have a significant effect on the initiation of plumes. For Earth, they are likely to change considerably and consistently on a global scale, both in time and space (Matthews et al., 2016). Consequently, neither coherent slabs nor a constant lateral TBL flow (magnitude and direction) are likely to occur in Earth over long periods of time. Thus, we may expect the Earth's lower mantle to be in a kind of adjustment stage for most of Earth's history, making it difficult to reach a state of globally long-term periodic plume generation as we observe it for constant or periodic plate velocities and fixed subduction zones. On the other hand, subducted slabs will be transformed into a broad belt of downwelling in the lowermost mantle (compare seismic tomography, e.g. in Figure 1), partially aided by the low viscosity of post-bridgmanite (Ammann et al., 2010) that is expected to be present in subducted slabs. Consequently, changes in plate configuration at the surface will most likely be significantly damped for the lowermost mantle, only resulting in comparably small changes in the strength of lateral flow along the CMB. Therefore, long-term stability of a degree-2 structure for flow in the lowermost mantle (Conrad et al., 2013; Torsvik et al., 2016) may locally allow for periodic plume initiation.

In either case, our proposed mechanism of plume initiation due to pile collapse may still be dominant for the initiation of individual plumes at various parts of the LLSVP margins. One example where this process may be especially relevant is the clustering of LIPs in the southeastern corner of the African LLSVP mentioned above (Figure 1), where at least 8 plumes erupted within about 60 Myr (Torsvik et al., 2016; Torsvik, 2019). Such a sequence might be explained by a large-scale collapse of a pile corner, which would lead to material spreading radially away from the pile interior. In this case, several plumes would be triggered in close spatial proximity around the collapsing and extending pile corner at approximately the same time, although small time delays and differences in rise time are very likely to occur. The collapse could be related to a significant reduction in the CMB flow, e.g. a reduction in plate velocity or change in TBL flow direction due to a modified configuration for the respective subduction zone(s) at the surface. If a subduction zone above an area of persistent downwelling changes its configuration (geometry, subduction velocity), this may cause a change in sinking velocity of the whole column and thus modify lateral TBL flow on shorter time scales than it takes slabs to sink through the whole mantle. In fact, plate reconstructions show a subduction zone closing in around the southern margin of Gondwana during the breakup of Pangaea between 250 Ma and 200 Ma, which then retreats between 200 Ma and 100 Ma (Matthews et al., 2016). The first stage would potentially result in increased TBL flow and pile thickness, while the retreating subduction zones would reduce TBL flow and may trigger a graviational collapse of the southeastern LLSVP egde. The delay between retreating subduction zones and the emplacement of LIPs at the surface (about 50-100 Myr together) can be explained by the reaction time of the deep mantle and the rise time of plumes.

7 Conclusions

In this study, we have shown that plumes at the core-mantle boundary can be triggered by two ways of increasing the thickness of the lower TBL. One is the conductive growth of the boundary layer, resulting in plumes appearing at random locations once the local Rayleigh number has exceeded a critical value (Deschamps & Tackley, 2008; M. Li & Zhong, 2017). This sets a minimum "natural" period $\mathcal{T}_{\mathrm{TBL}}$ at which plumes are generated from the CMB, but does not necessarily represent the observed period in the presence of a thermochemical pile.

The other mechanism is a periodic gravitational collapse of the edge of a thermochemical pile on the CMB. This collapse occurs as plumes locally thicken the pile when they interact with the pile margin, and resembles the vertical motion of tent-shaped piles observed by M. Li et al. (2018). When the increased pile thickness is no longer supported due to cooling of the pile top and reduced dynamic uplift from the rising plume, the pile margin collapses back towards the CMB and spreads laterally. This process pushes TBL material against the dominant flow direction and causes local thickening of the TBL just outside the thermochemical pile, triggering a new "early" plume.

The period of this pile collapse, $\mathcal{T}_{\mathrm{Pile}}$, depends on the mantle wind along the CMB, which is controlled by the temperature-dependence of viscosity (which affects the sinking velocity of slabs) and velocity with which plates are subducted. The latter can modify the observed plume period, but shorter periods resulting from faster plate velocities reduce plume strength. For periodic plate velocities, plume periods can adjust to imposed plate cycles within a certain resonance range around the characteristic period $\mathcal{T}_{\mathrm{Pile}}$. For $\mathcal{T}_{\mathrm{TBL}} > \mathcal{T}_{\mathrm{Pile}}$, plumes are predominantly initated at the pile margin and their effectively observed period is $\mathcal{T}_{\mathrm{Pile}}$, with potentially weak plumes for $\mathcal{T}_{\mathrm{TBL}} \gg \mathcal{T}_{\mathrm{Pile}}$. In contrast $\mathcal{T}_{\mathrm{TBL}} < \mathcal{T}_{\mathrm{Pile}}$ causes plume initiation both at the pile margins and away from them, resulting in aperiodic behaviour.

Although there is currently insufficient data from LIPs or hotspots to infer a cyclicity in plume initiation within Earth's mantle, we would estimate the Earth to be in the regime of $\mathcal{T}_{\mathrm{TBL}} \gtrsim \mathcal{T}_{\mathrm{Pile}}$ since most LIPs/ hotspots are clustered around the LLSVP margins. Yet, plumes must be strong enough to reach the surface, presumably excluding "very early" plume initiation ($\mathcal{T}_{\mathrm{TBL}} \gg \mathcal{T}_{\mathrm{Pile}}$). Finally, the mechanism for plume generation at the edges of thermochemical piles may explain the observed clustering of LIPs between 95 Ma and 155 Ma at the southeastern corner of the African LLSVP.

Acknowledgments

We thank Trond Torsvik for valuable discussions, as well as the editor Stephen Parman, Mingming Li and three anonymous reviewers for comments and suggestions that helped to improve the manuscript. Input parameters for numerical models can be found in Table 1 and Table 2, the code ASPECT v.2.0.1 is available from (Bangerth et al., 2018) and the data of LIPs are given in (Torsvik, 2019). This work was supported by the Research Council of Norway Centres of Excellence project 223272 and through the Norwegian Research School DEEP project 249040/F60. Computation time was provided by the Norwegian computational infrastructure (sigma2) via allocations NN9283K/ NS9029K. We thank the Computational Infrastructure for Geodynamics (geodynamics.org), which is funded by the National Science Foundation under award EAR-0949446 and EAR-1550901, for supporting the development of ASPECT.

References

Ammann, M. W., Brodholt, J. P., Wookey, J., & Dobson, D. P. (2010, May). First-principles constraints on diffusion in lower-mantle minerals and a weak d layer. *Nature*, *465*, 462–465. Retrieved from `https://www.nature.com/articles/nature09052\#supplementary-information` doi: 10.1038/nature09052;10.1038/nature09052

Andersen, M. B., Elliott, T., Freymuth, H., Sims, K. W. W., Niu, Y., & Kelley, K. A. (2015). The terrestrial uranium isotope cycle. *Nature*, *517*(7534), 356–359. doi: 10.1038/nature14062;10.1038/nature14062

Austermann, J., Kaye, B. T., Mitrovica, J. X., & Huybers, P. (2014, 01). A statistical analysis of the correlation between large igneous provinces and lower mantle seismic structure. *Geophysical Journal International*, *197*(1), 1–9. Retrieved from `https://doi.org/10.1093/gji/ggt500` doi: 10.1093/gji/ggt500

Ballmer, M. D., Schmerr, N. C., Nakagawa, T., & Ritsema, J. (2015). Compositional mantle layering revealed by slab stagnation at 1000-km depth. *Science Advances*, *1*(11). Retrieved from `https://advances.sciencemag.org/content/1/11/e1500815` doi: 10.1126/sciadv.1500815

Ballmer, M. D., Schumacher, L., Lekic, V., Thomas, C., & Ito, G. (2016). Compositional layering within the large low shear-wave velocity provinces in the lower mantle. *Geochemistry, Geophysics, Geosystems*, *17*(12), 5056–5077. Retrieved from `https://agupubs.onlinelibrary.wiley.com/doi/abs/10.1002/2016GC006605` doi: 10.1002/2016GC006605

Bangerth, W., Dannberg, J., Gassmoeller, R., Heister, T., et al. (2018, June). *ASPECT v2.0.1 [software].* Davis, CA. Retrieved from `https://doi.org/10.5281/zenodo.1297145` doi: 10.5281/zenodo.1297145

Bangerth, W., Dannberg, J., Gassmöller, R., Heister, T., et al. (2019, April). ASPECT: Advanced solver for problems in earth's convection, user manual. Retrieved from `https://doi.org/10.6084/m9.figshare.4865333` (doi:10.6084/m9.figshare.4865333) doi: 10.6084/m9.figshare.4865333

Christensen, U. R., & Hofmann, A. W. (1994). Segregation of subducted oceanic crust in the convecting mantle. *Journal of Geophysical Research: Solid Earth*, *99*(B10), 19867–19884. Retrieved from `https://agupubs.onlinelibrary.wiley.com/doi/abs/10.1029/93JB03403` doi: 10.1029/93JB03403

Conrad, C. P., Steinberger, B., & Torsvik, T. H. (2013, June). Stability of active mantle upwelling revealed by net characteristics of plate tectonics. *Nature*, *498*, 479–482. Retrieved from `https://www.nature.com/articles/nature12203\#supplementary-information` doi: 10.1038/nature12203;10.1038/nature12203

Cottaar, S., & Lekic, V. (2016, 08). Morphology of seismically slow lower-mantle structures. *Geophysical Journal International*, *207*(2), 1122–1136. Retrieved from `https://doi.org/10.1093/gji/ggw324` doi: 10.1093/gji/ggw324

Dannberg, J., & Gassmöller, R. (2018). Chemical trends in ocean islands explained by plume–slab interaction. *Proceedings of the National Academy of Sciences*, *115*(17), 4351–4356. Retrieved from `https://www.pnas.org/content/115/17/4351` doi: 10.1073/pnas.1714125115

Dannberg, J., & Sobolev, S. V. (2015, April). Low-buoyancy thermochemical plumes resolve controversy of classical mantle plume concept. *Nature Communications*, *6*, 6960. Retrieved from https://www.nature.com/articles/ncomms7960\#supplementary-information doi: 10.1038/ncomms7960;10.1038/ncomms7960

Davaille, A., Girard, F., & Bars, M. L. (2002). How to anchor hotspots in a convecting mantle? *Earth and Planetary Science Letters*, *203*(2), 621–634. Retrieved from http://www.sciencedirect.com/science/article/pii/S0012821X0200897X doi: 10.1016/S0012-821X(02)00897-X

Davies, D. R., Goes, S., Davies, J., Schuberth, B., Bunge, H.-P., & Ritsema, J. (2012). Reconciling dynamic and seismic models of earth's lower mantle: The dominant role of thermal heterogeneity. *Earth and Planetary Science Letters*, *353-354*, 253–269. Retrieved from http://www.sciencedirect.com/science/article/pii/S0012821X1200444X doi: 10.1016/j.epsl.2012.08.016

Davies, D. R., Goes, S., & Sambridge, M. (2015). On the relationship between volcanic hotspot locations, the reconstructed eruption sites of large igneous provinces and deep mantle seismic structure. *Earth and Planetary Science Letters*, *411*, 121–130. Retrieved from http://www.sciencedirect.com/science/article/pii/S0012821X14007523 doi: 10.1016/j.epsl.2014.11.052

Deschamps, F., & Tackley, P. J. (2008). Searching for models of thermo-chemical convection that explain probabilistic tomography: I. principles and influence of rheological parameters. *Physics of the Earth and Planetary Interiors*, *171*(1), 357–373. Retrieved from http://www.sciencedirect.com/science/article/pii/S0031920108000824 (Recent Advances in Computational Geodynamics: Theory, Numerics and Applications) doi: 10.1016/j.pepi.2008.04.016

Doubrovine, P. V., Steinberger, B., & Torsvik, T. H. (2016). A failure to reject: Testing the correlation between large igneous provinces and deep mantle structures with edf statistics. *Geochemistry, Geophysics, Geosystems*, *17*(3), 1130–1163. Retrieved from https://agupubs.onlinelibrary.wiley.com/doi/abs/10.1002/2015GC006044 doi: 10.1002/2015GC006044

Dziewonski, A. M., Lekic, V., & Romanowicz, B. A. (2010). Mantle anchor structure: An argument for bottom up tectonics. *Earth and Planetary Science Letters*, *299*(1), 69–79. Retrieved from http://www.sciencedirect.com/science/article/pii/S0012821X10005236 doi: 10.1016/j.epsl.2010.08.013

Farnetani, C. G., Hofmann, A. W., Duvernay, T., & Limare, A. (2018). Dynamics of rheological heterogeneities in mantle plumes. *Earth and Planetary Science Letters*, *499*, 74–82. Retrieved from `http://www.sciencedirect.com/science/article/pii/S0012821X1830428X` doi: 10.1016/j.epsl.2018.07.022

French, S. W., & Romanowicz, B. (2015, September). Broad plumes rooted at the base of the earth's mantle beneath major hotspots. *Nature*, *525*, 95. Retrieved from `https://www.nature.com/articles/nature14876\#supplementary-information` doi: 10.1038/nature14876;10.1038/nature14876

Garnero, E. J., & McNamara, A. K. (2008). Structure and dynamics of earth's lower mantle. *Science*, *320*(5876), 626–628. Retrieved from `https://science.sciencemag.org/content/320/5876/626` doi: 10.1126/science.1148028

Garnero, E. J., McNamara, A. K., & Shim, S.-H. (2016, June). Continent-sized anomalous zones with low seismic velocity at the base of earth's mantle. *Nature Geoscience*, *9*, 481–489. Retrieved from `https://www.nature.com/articles/ngeo2733\#supplementary-information` doi: 10.1038/ngeo2733;10.1038/ngeo2733

Hager, B. H., Clayton, R. W., Richards, M. A., Comer, R. P., & Dziewonski, A. M. (1985). Lower mantle heterogeneity, dynamic topography and the geoid. *Nature*, *313*(6003), 541–545. doi: 10.1038/313541a0;10.1038/313541a0

He, Y., Puckett, E. G., & Billen, M. I. (2017). A discontinuous Galerkin method with a bound preserving limiter for the advection of non-diffusive fields in solid earth geodynamics. *Physics of the Earth and Planetary Interiors*, *263*, 23–37. Retrieved from `https://doi.org/10.1016/j.pepi.2016.12.001` doi: 10.1016/j.pepi.2016.12.001

Heister, T., Dannberg, J., Gassmöller, R., & Bangerth, W. (2017). High accuracy mantle convection simulation through modern numerical methods. II: Realistic models and problems. *Geophysical Journal International*, *210*(2), 833–851. Retrieved from `https://doi.org/10.1093/gji/ggx195` doi: 10.1093/gji/ggx195

Heyn, B. H., Conrad, C. P., & Trønnes, R. G. (2018). Stabilizing effect of compositional viscosity contrasts on thermochemical piles. *Geophysical Research Letters*, *45*(15), 7523–7532. Retrieved from `https://agupubs.onlinelibrary`

.wiley.com/doi/abs/10.1029/2018GL078799 doi: 10.1029/2018GL078799

Hirose, K., Takafuji, N., Sata, N., & Ohishi, Y. (2005). Phase transition and density of subducted morb crust in the lower mantle. *Earth and Planetary Science Letters*, *237*(1), 239–251. Retrieved from http://www.sciencedirect.com/science/article/pii/S0012821X0500419X doi: 10.1016/j.epsl.2005.06.035

Howard, L. N. (1966). Convection at high rayleigh number. In H. Görtler (Ed.), *Applied mechanics* (pp. 1109–1115). Berlin, Heidelberg: Springer Berlin Heidelberg.

Jones, T. D., Davies, D., Campbell, I., Wilson, C., & Kramer, S. (2016). Do mantle plumes preserve the heterogeneous structure of their deep-mantle source? *Earth and Planetary Science Letters*, *434*, 10–17. Retrieved from http://www.sciencedirect.com/science/article/pii/S0012821X15007141 doi: 10.1016/j.epsl.2015.11.016

King, S. D., & Adam, C. (2014). Hotspot swells revisited. *Physics of the Earth and Planetary Interiors*, *235*, 66–83. Retrieved from http://www.sciencedirect.com/science/article/pii/S0031920114001642 doi: 10.1016/j.pepi.2014.07.006

Koelemeijer, P. J., Deuss, A., & Ritsema, J. (2017, May). Density structure of earth's lowermost mantle from stoneley mode splitting observations. *Nature Communications*, *8*, 15241. Retrieved from https://www.nature.com/articles/ncomms15241\#supplementary-information doi: 10.1038/ncomms15241;10.1038/ncomms15241

Koelemeijer, P. J., Schuberth, B., Davies, D., Deuss, A., & Ritsema, J. (2018). Constraints on the presence of post-perovskite in earth's lowermost mantle from tomographic-geodynamic model comparisons. *Earth and Planetary Science Letters*, *494*, 226–238. Retrieved from http://www.sciencedirect.com/science/article/pii/S0012821X18302656 doi: 10.1016/j.epsl.2018.04.056

Kronbichler, M., Heister, T., & Bangerth, W. (2012). High accuracy mantle convection simulation through modern numerical methods. *Geophysical Journal International*, *191*, 12–29. Retrieved from http://dx.doi.org/10.1111/j.1365-246X.2012.05609.x doi: 10.1111/j.1365-246X.2012.05609.x

Labrosse, S., Hernlund, J. W., & Coltice, N. (2007, December). A crystallizing dense magma ocean at the base of the earth's mantle. *Nature*, *450*, 866–

869. Retrieved from https://www.nature.com/articles/nature06355\#supplementary-information doi: 10.1038/nature06355;10.1038/nature06355

Lau, H. C. P., Mitrovica, J. X., Davis, J. L., Tromp, J., Yang, H.-Y., & Al-Attar, D. (2017, November). Tidal tomography constrains earth's deep-mantle buoyancy. *Nature*, *551*, 321–326. doi: 10.1038/nature24452;10.1038/nature24452

Lay, T. (2015). 1.22 - deep earth structure: Lower mantle and d. In G. Schubert (Ed.), *Treatise on geophysics (second edition)* (Second Edition ed., pp. 683–723). Oxford: Elsevier. Retrieved from http://www.sciencedirect.com/science/article/pii/B9780444538024000191 doi: 10.1016/B978-0-444-53802-4.00019-1

Lekic, V., Cottaar, S., Dziewonski, A., & Romanowicz, B. (2012). Cluster analysis of global lower mantle tomography: A new class of structure and implications for chemical heterogeneity. *Earth and Planetary Science Letters*, *357-358*, 68–77. Retrieved from http://www.sciencedirect.com/science/article/pii/S0012821X12005109 doi: 10.1016/j.epsl.2012.09.014

Li, M., & McNamara, A. K. (2013). The difficulty for subducted oceanic crust to accumulate at the earth's core-mantle boundary. *Journal of Geophysical Research: Solid Earth*, *118*(4), 1807–1816. Retrieved from https://agupubs.onlinelibrary.wiley.com/doi/abs/10.1002/jgrb.50156 doi: 10.1002/jgrb.50156

Li, M., McNamara, A. K., & Garnero, E. J. (2014, March). Chemical complexity of hotspots caused by cycling oceanic crust through mantle reservoirs. *Nature Geoscience*, *7*, 366–370. Retrieved from https://www.nature.com/articles/ngeo2120\#supplementary-information doi: 10.1038/ngeo2120;10.1038/ngeo2120

Li, M., & Zhong, S. (2017). The source location of mantle plumes from 3d spherical models of mantle convection. *Earth and Planetary Science Letters*, *478*, 47–57. Retrieved from http://www.sciencedirect.com/science/article/pii/S0012821X17304806 doi: 10.1016/j.epsl.2017.08.033

Li, M., Zhong, S., & Olson, P. (2018). Linking lowermost mantle structure, core-mantle boundary heat flux and mantle plume formation. *Physics of the Earth and Planetary Interiors*, *277*, 10–29. Retrieved from http://

www.sciencedirect.com/science/article/pii/S0031920117302625 doi: 10.1016/j.pepi.2018.01.010

Li, Y., Deschamps, F., & Tackley, P. J. (2014, 09). The stability and structure of primordial reservoirs in the lower mantle: insights from models of thermochemical convection in three-dimensional spherical geometry. *Geophysical Journal International*, *199*(2), 914–930. Retrieved from https://doi.org/10.1093/gji/ggu295 doi: 10.1093/gji/ggu295

Li, Y., Deschamps, F., & Tackley, P. J. (2015). Effects of the post-perovskite phase transition properties on the stability and structure of primordial reservoirs in the lower mantle of the earth. *Earth and Planetary Science Letters*, *432*, 1–12. Retrieved from http://www.sciencedirect.com/science/article/pii/S0012821X15006159 doi: 10.1016/j.epsl.2015.09.040

Matthews, K. J., Maloney, K. T., Zahirovic, S., Williams, S. E., Seton, M., & Müller, R. D. (2016). Global plate boundary evolution and kinematics since the late paleozoic. *Global and Planetary Change*, *146*, 226–250. Retrieved from http://www.sciencedirect.com/science/article/pii/S0921818116302417 doi: 10.1016/j.gloplacha.2016.10.002

McNamara, A. K., & Zhong, S. (2004). Thermochemical structures within a spherical mantle: Superplumes or piles? *Journal of Geophysical Research: Solid Earth*, *109*(B7). Retrieved from https://agupubs.onlinelibrary.wiley.com/doi/abs/10.1029/2003JB002847 doi: 10.1029/2003JB002847

McNamara, A. K., & Zhong, S. (2005). Thermochemical structures beneath africa and the pacific ocean. *Nature*, *437*(7062), 1136–1139. doi: 10.1038/nature04066;10.1038/nature04066

Moulik, P., & Ekström, G. (2016). The relationships between large-scale variations in shear velocity, density, and compressional velocity in the earth's mantle. *Journal of Geophysical Research: Solid Earth*, *121*(4), 2737–2771. Retrieved from https://agupubs.onlinelibrary.wiley.com/doi/abs/10.1002/2015JB012679 doi: 10.1002/2015JB012679

Mulyukova, E., Steinberger, B., Dabrowski, M., & Sobolev, S. V. (2015). Survival of llsvps for billions of years in a vigorously convecting mantle: Replenishment and destruction of chemical anomaly. *Journal of Geophysical Research: Solid Earth*, *120*(5), 3824–3847. Retrieved from https://

agupubs.onlinelibrary.wiley.com/doi/abs/10.1002/2014JB011688 doi: 10.1002/2014JB011688

Nakagawa, T., & Tackley, P. J. (2011). Effects of low-viscosity post-perovskite on thermo-chemical mantle convection in a 3-d spherical shell. *Geophysical Research Letters*, *38*(4). Retrieved from https://agupubs.onlinelibrary.wiley.com/doi/abs/10.1029/2010GL046494 doi: 10.1029/2010GL046494

Romanowicz, B. (2003). Global mantle tomography: Progress status in the past 10 years. *Annual Review of Earth and Planetary Sciences*, *31*(1), 303–328. Retrieved from https://doi.org/10.1146/annurev.earth.31.091602.113555 doi: 10.1146/annurev.earth.31.091602.113555

Schuberth, B. S. A., Bunge, H.-P., & Ritsema, J. (2009). Tomographic filtering of high-resolution mantle circulation models: Can seismic heterogeneity be explained by temperature alone? *Geochemistry, Geophysics, Geosystems*, *10*(5). Retrieved from https://agupubs.onlinelibrary.wiley.com/doi/abs/10.1029/2009GC002401 doi: 10.1029/2009GC002401

Schuberth, B. S. A., Bunge, H.-P., Steinle-Neumann, G., Moder, C., & Oeser, J. (2009). Thermal versus elastic heterogeneity in high-resolution mantle circulation models with pyrolite composition: High plume excess temperatures in the lowermost mantle. *Geochemistry, Geophysics, Geosystems*, *10*(1). Retrieved from https://agupubs.onlinelibrary.wiley.com/doi/abs/10.1029/2008GC002235 doi: 10.1029/2008GC002235

Schuberth, B. S. A., Zaroli, C., & Nolet, G. (2012, 03). Synthetic seismograms for a synthetic earth: long-period p- and s-wave traveltime variations can be explained by temperature alone. *Geophysical Journal International*, *188*(3), 1393–1412. Retrieved from https://doi.org/10.1111/j.1365-246X.2011.05333.x doi: 10.1111/j.1365-246X.2011.05333.x

Steinberger, B., & Torsvik, T. H. (2012). A geodynamic model of plumes from the margins of large low shear velocity provinces. *Geochemistry, Geophysics, Geosystems*, *13*(1). Retrieved from https://agupubs.onlinelibrary.wiley.com/doi/abs/10.1029/2011GC003808 doi: 10.1029/2011GC003808

Tackley, P. J. (2012). Dynamics and evolution of the deep mantle resulting from thermal, chemical, phase and melting effects. *Earth-Science Reviews*, *110*(1), 1–25. Retrieved from http://www.sciencedirect.com/science/article/

pii/S0012825211001486 doi: 10.1016/j.earscirev.2011.10.001

Tan, E., Leng, W., Zhong, S., & Gurnis, M. (2011). On the location of plumes and lateral movement of thermochemical structures with high bulk modulus in the 3-d compressible mantle. *Geochemistry, Geophysics, Geosystems*, *12*(7). Retrieved from https://agupubs.onlinelibrary.wiley.com/doi/abs/10.1029/2011GC003665 doi: 10.1029/2011GC003665

Torsvik, T. H. (2019). Earth history: A journey in time and space from base to top. *Tectonophysics*, *760*, 297–313. Retrieved from http://www.sciencedirect.com/science/article/pii/S0040195118303147 (Linking Plate Tectonics and Volcanism to Deep Earth Dynamics – a tribute to Trond H. Torsvik) doi: 10.1016/j.tecto.2018.09.009

Torsvik, T. H., Burke, K., Steinberger, B., Webb, S. J., & Ashwal, L. D. (2010, July). Diamonds sampled by plumes from the core–mantle boundary. *Nature*, *466*, 352–355. Retrieved from https://www.nature.com/articles/nature09216\#supplementary-information doi: 10.1038/nature09216;10.1038/nature09216

Torsvik, T. H., Smethurst, M. A., Burke, K., & Steinberger, B. (2006). Large igneous provinces generated from the margins of the large low-velocity provinces in the deep mantle. *Geophysical Journal International*, *167*(3), 1447–1460. Retrieved from https://onlinelibrary.wiley.com/doi/abs/10.1111/j.1365-246X.2006.03158.x doi: 10.1111/j.1365-246X.2006.03158.x

Torsvik, T. H., Steinberger, B., Ashwal, L. D., Doubrovine, P. V., & Trønnes, R. G. (2016). Earth evolution and dynamics—a tribute to kevin burke. *Canadian Journal of Earth Sciences*, *53*(11), 1073–1087. Retrieved from https://doi.org/10.1139/cjes-2015-0228 doi: 10.1139/cjes-2015-0228

Trønnes, R. G., Baron, M., Eigenmann, K., Guren, M., Heyn, B., Løken, A., & Mohn, C. (2019). Core formation, mantle differentiation and core-mantle interaction within earth and the terrestrial planets. *Tectonophysics*, *760*, 165–198. Retrieved from http://www.sciencedirect.com/science/article/pii/S0040195118303494 (Linking Plate Tectonics and Volcanism to Deep Earth Dynamics – a tribute to Trond H. Torsvik) doi: 10.1016/j.tecto.2018.10.021

Table 1. Characteristic parameters for thermochemical calculations. For the conversion of dimensional excess densities, given in the input parameters of the simulations, into B (equation (3)), we assume a temperature drop across the mantle of 3300 K, which includes both the 2300 K superadiabatic temperature drop that we have used in our models with Boussinesq approximation, and an adiabatic temperature increase of 1000 K. Furthermore, although our model has a constant value of $\alpha = 3.0 \cdot 10^{-5}$ for the whole mantle, we use a thermal expansivity of $\alpha = 1.0 \cdot 10^{-5}$ at the CMB (Tackley, 2012) for conversion to B. Buoyancy ratios obtained with these parameters are more easily comparable to previous studies (e.g., McNamara & Zhong, 2004; Mulyukova et al., 2015; Heyn et al., 2018) and applicable to Earth. Ra is also calculated using the full temperature drop of 3300 K to make it comparable to previous studies and has a value of 10^7 from the parameters below. ASPECT uses thermal conductivity k and specific heat capacity c_P instead of thermal diffusvity κ, but the latter can be calculated via $\kappa = \frac{k}{\rho c_P}$ and equals $1.0 \cdot 10^{-6}$ [m^2/s].

Parameter	Symbol	Value [Unit]
Gravitational acceleration	g	9.81 [m/s^2]
Mantle thickness	d	2890 [km]
Reference density	ρ	3340 [kg/m^3]
Reference viscosity	η	$7.83 \cdot 10^{21}$ [Pa·s]
Thermal conductivity	k	4.01 [W/K·m]
Specific heat	c_P	1200 [kg·m^2/(K·s^2)]
Thermal expansivity	α	$3.0 \cdot 10^{-5}$ [1/K]
Chemical excess density	$\Delta\rho_C$	198.396 – 330.66 [kg/m^3]
Activation energy	E_a	27436.2 – 32923.44 [J/mol]
Buoyancy ratio (eq. (3))	B	0.6 – 1.0 [ ]
Rayleigh number	Ra	10^7 [ ]
Internal heating rate	H	$9.46 \cdot 10^{-13}$ [W/kg]
Imposed surface velocity	v_{surf}	0.74-2.96 [cm/yr]
Compositional viscosity contrast	η_C	1 – 20 [ ]
Thermal viscosity contrast	$\eta_{\Delta T}$	2.3 – 55000 [ ]
Temperature drop across mantle	ΔT	2300 [K]

Table 2. Parameters defining the viscosity profiles according to the thermal viscosity contrast $\eta_{\Delta T}$. Steps for the non-dimensional activation energy E_η (converted via $E_\eta = \frac{E_a}{R\Delta T}$, with the gas constant R and the temperature drop as described in Table 1), the temperature offset T_η and the viscosity prefactor η_0 are set at depths of 299 km (lithosphere-asthenosphere boundary), 410 km (upper mantle - transition zone) and 660 km (transition zone - lower mantle). Values are sorted by increasing depth.

$\eta_{\Delta T}$	η_0	E_η	T_η
2.3	5 / 0.5 / 2.5 / 5	1 / 1 / 1 / 1	0.02 / 0.4 / 0.6 / 0.7
65	5 / 0.5 / 2.5 / 5	1 / 1 / 1 / 1	0.02 / 0.2 / 0.2 / 0.2
330	5 / 0.5 / 2.5 / 5	1 / 1 / 1 / 1	0.02 / 0.15 / 0.15 / 0.15
1700	5 / 0.5 / 2.5 / 5	1 / 1 / 1 / 1	0.02 / 0.12 / 0.12 / 0.12
7500	5 / 0.5 / 2.5 / 5	1.2 / 1.2 / 1.2 / 1.2	0.02 / 0.12 / 0.12 / 0.12
55000	5 / 0.5 / 2.5 / 5	1.2 / 1.2 / 1.2 / 1.2	0.02 / 0.1 / 0.1 / 0.1

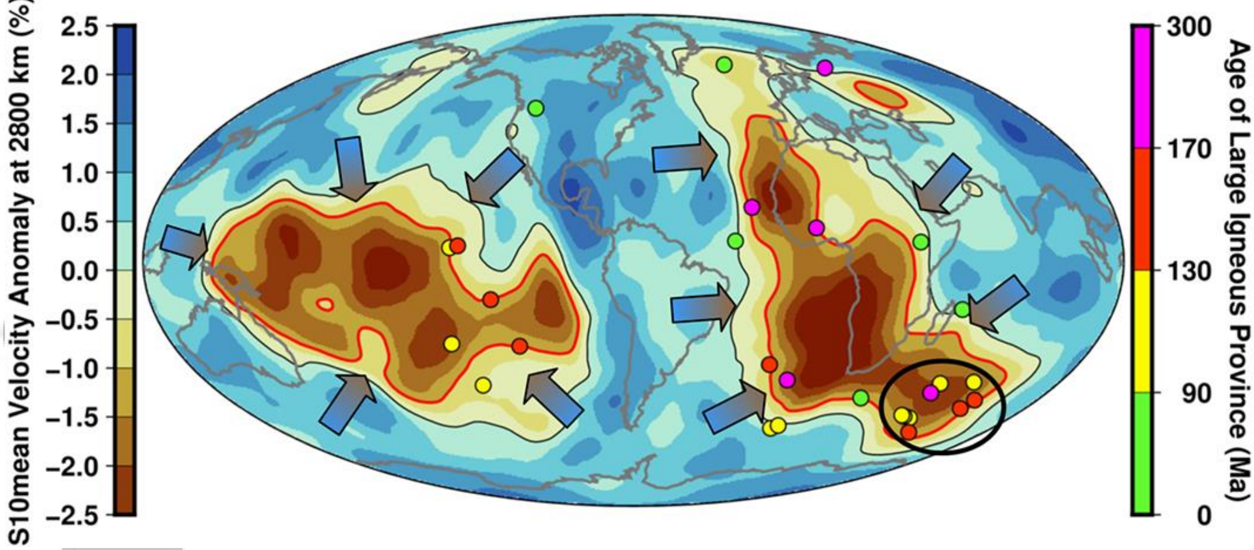

Figure 1. Distribution of reconstructed eruption sites of LIPs (Torsvik, 2019) around the two Large Low Shear Wave Velocity Provinces (LLSVPs) indicated by velocity anomalies of the S10mean shear wave tomography model of Doubrovine et al. (2016). Contour lines are drawn for 0.0% (black) and -1.0% (red) velocity anomalies. Reconstructed eruption sites of LIPs are marked by circles, with color corresponding to age. There is a cluster of 9 LIPs around the southeastern corner of the African LLSVP (marked by black circle), of which 8 erupted between 155-95 Ma (red and yellow circles) and one at 285 Ma (purple circle). Thick arrows indicate the inferred steady flow from the circumpolar belt of subducted material towards the LLSVPs.

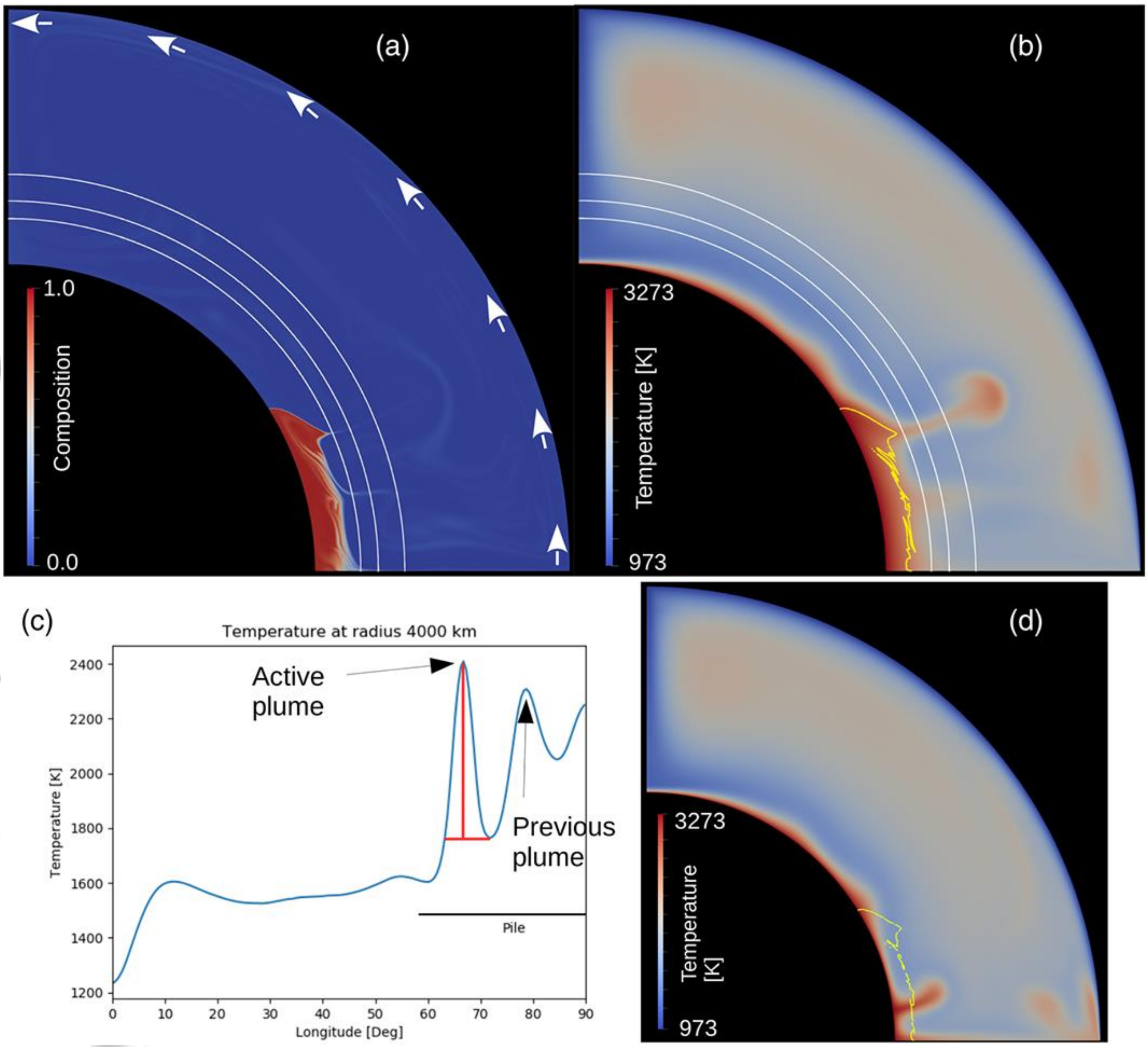

Figure 2. Initial condition for (a) composition field and (b) temperature field, with radii of 4000 km, 4200 km and 4500 km marked as white lines. Profiles along these radii are used to identify and investigate plumes. White arrows in (a) indicate the imposed plate velocity, while the yellow line in (b) marks the outline of the dense pile for a countour line of composition at $C = 0.8$. (c) An example of a temperature profile along the radius of 4000 km for the initial condition shown in (b). Identified plumes are marked with black arrows. The width and the excess temperature we obtain are marked with red lines for one of the plumes. The black horizontal line indicates the part of the CMB that is covered by the pile. Panel (d) shows a snapshot of the temperature field for our isochemical test case with $\eta_{\Delta T} = 330$. Even though thermal instabilities become visible at approximately the same longitude as the edge of piles in thermochemical models (indicated by the yellow line), plumes only finally start to rise closer to the domain boundary.

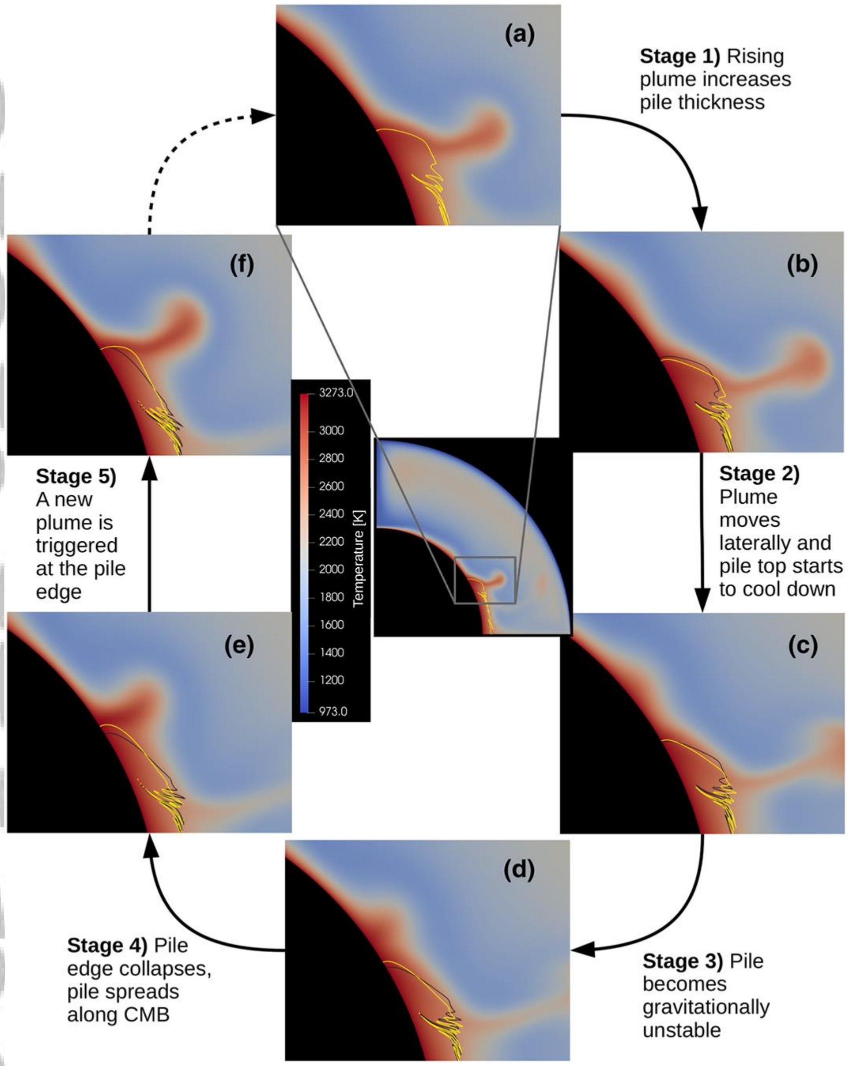

Figure 3. Snapshots of the temperature field around the pile edge during the plume cycle for our reference model ($B = 0.8$, $\eta_C = 10$ and $\eta_{\Delta T} = 330$). Yellow lines show the outline of the dense material ($C = 0.8$) at the current time step, while grey lines indicate the shape of the pile in the previous snapshot for comparison. As can be seen, the plume increases local pile thickness and drives a pile-ward a motion of the pile edge (stages 1 and 2) until the plume can no longer support the thicker pile, which starts to collapse back towards the CMB, where it spreads against the push of the slab (stages 3 and 4). This results in a local thickening of the thermal boundary layer outside the pile, which triggers the next plume (stage 5). In some cases, the next thermal instability may already be identified as thickened boundary layer before arrival at the pile margin (b and c), although the TBL directly next to the pile has been emptied by the previous active plume and therefore thinned. The pile collapse finally increases the TBL thickness sufficiently to actually trigger the plume at the pile margin. The plume cycle is also shown in Movie S1 for the same model. Plume rise times are discussed in more detail in section 6.1.

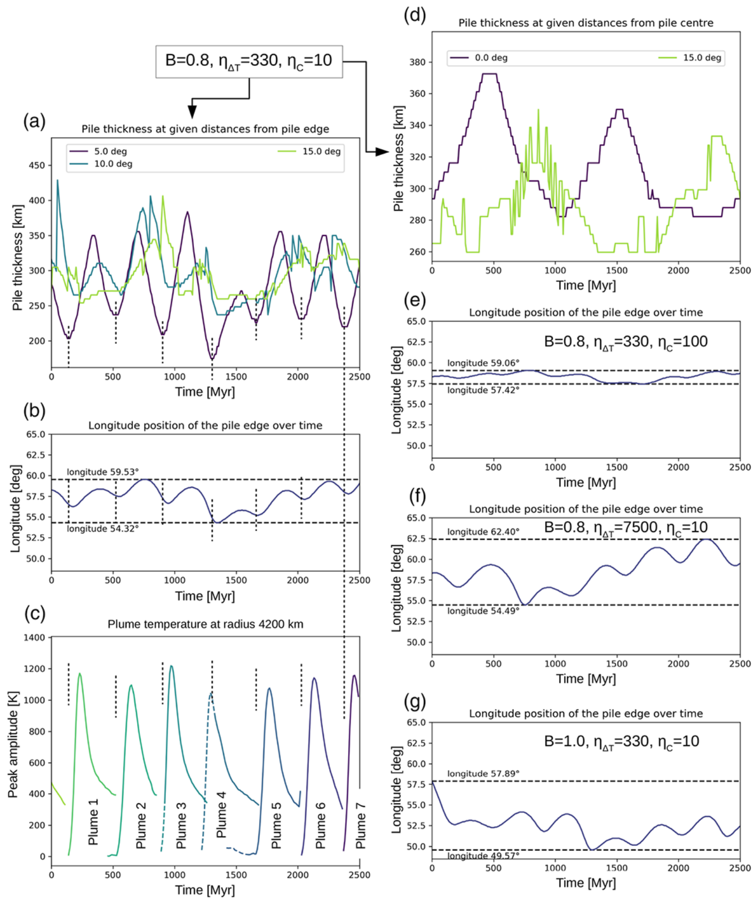

Figure 4. The plume cycle for our reference model with $B = 0.8$, $\eta_C = 10$ and $\eta_{\Delta T} = 330$ and a constant plate velocity of 1.48 cm/year can be identified in variations of pile thickness inwards from the pile edge, especially at 5 degrees inwards (a), the lateral motion of the pile edge (b) and the excess temperature of upwellings at a radius of 4200 km (c). As can be seen by the black dotted lines, every minimum in pile thickness and edge longitude corresponds to a plume in (c), although there is a small time difference between the three graphs that represents a delay in reaction between pile and plume. In contrast, the plume cycle is not represented in pile thickness close to the pile centre (d). Sharp changes in pile thickness (especially observed for the pile centre) are related to the ragged top of the pile (see Figure 2). (e)-(g) show the motions of the pile edge for models with increased compositional viscosity contrast (e), increased thermal viscosity contrast (f) and increased density (g), but otherwise the same parameters as the reference model. Note the change in the longitude range of lateral pile edge motion associated with the changed parameters.

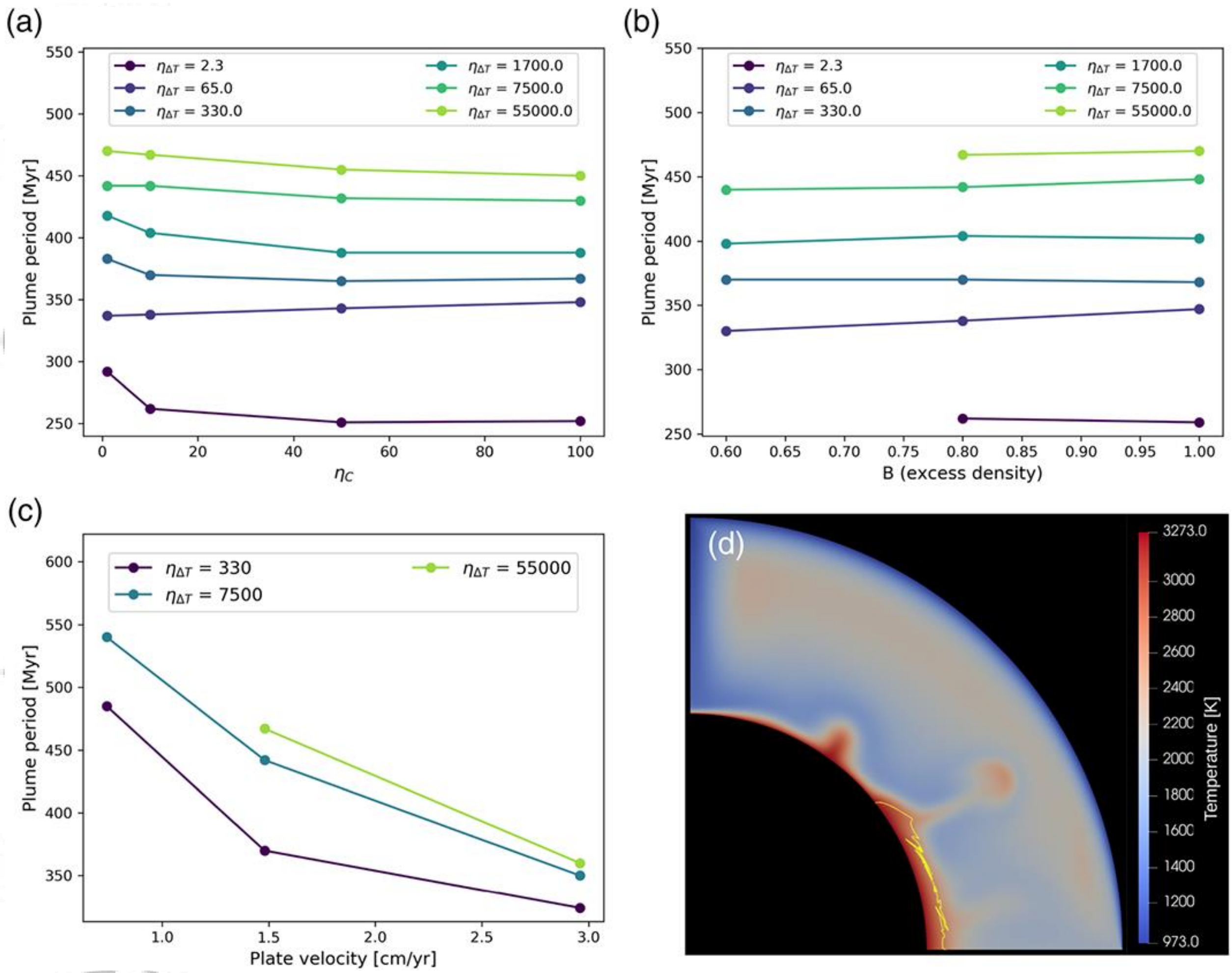

Figure 5. The period of the plume cycle for a plate velocity of $v_{\text{surf}} = 1.48\,\text{cm/year}$ as a function of (a) the compositional viscosity contrast η_C for $B = 0.8$, (b) the density contrast B for $\eta_C = 10$ and (c) the plate velocity for $B = 0.8$ and $\eta_C = 10$. Models with different thermal viscosity contrasts $\eta_{\Delta T}$ are marked by the color of the line. Outliers in (b) and (c) for $\eta_{\Delta T} = 55000$ and the lowest density or velocity, respectively, fall outside the plotted area. As can be seen, neither η_C nor B have a strong effect on the period, while models with different $\eta_{\Delta T}$ are clearly separated from each other. The period of plumes increases significantly with increasing $\eta_{\Delta T}$. In additon, the period is strongly affected by the plate velocity. Especially for low velocities, plumes may also form independently of the the pile collapse, for example as in (d) with $B = 0.8$, $\eta_C = 10$, $\eta_{\Delta T} = 55000$ and a velocity of $0.74\,\text{cm/year}$. In this case, plumes initiated away from the pile tend to merge with those starting at the pile, making it difficult to determine plume characteristics such as the period shown in (c).

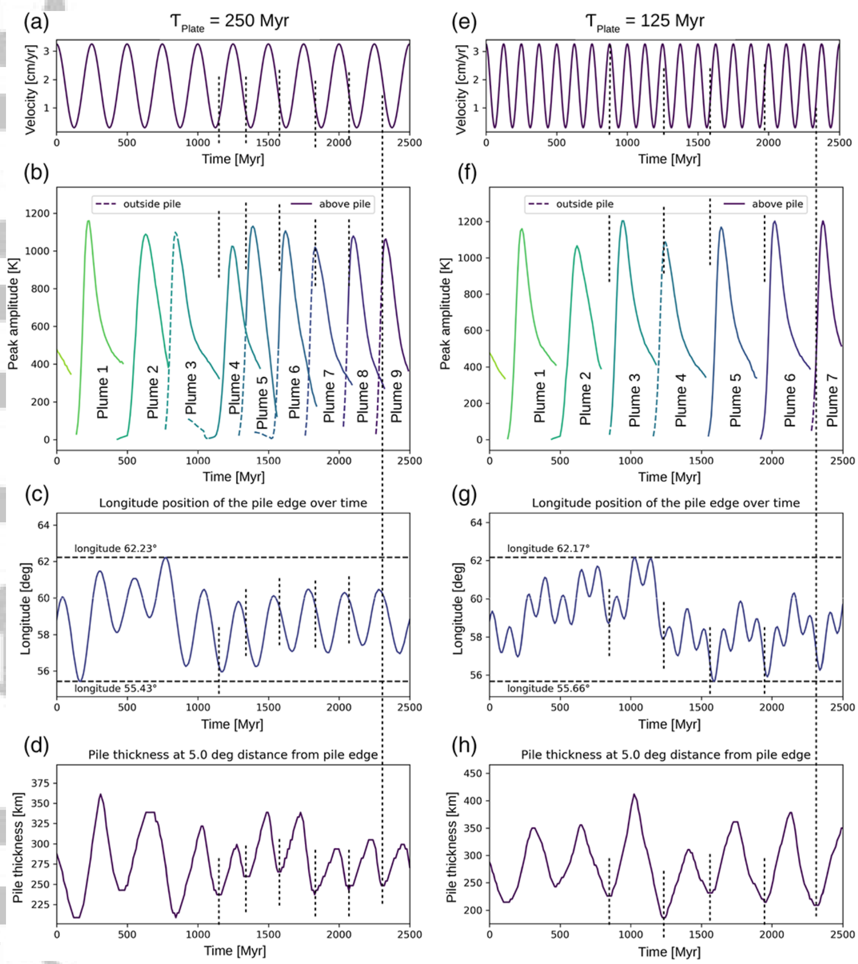

Figure 6. Representative characteristics of the plume cycle for models with $B = 0.8$, $\eta_C = 10$ and $\eta_{\Delta T} = 330$ and a periodic velocity boundary condition of $\mathcal{T}_{\text{Plate}} = 250\,\text{Myr}$ (left) and $\mathcal{T}_{\text{Plate}} = 125\,\text{Myr}$ (right). The top panels (a) and (e) indicate the plate velocity as reference, while panels (b) and (f) in the second row show the excess temperature of identified plumes at 4200 km radius. The third row with panels (c) and (g) and the lower panels (d) and (h) illustrate the motion of the pile edge and the variation in pile thickness at a distance of 5 degrees inwards from the pile edge, respectively. As can be seen, both lateral pile edge motion and pile thickness reflect the plume cycle for $\mathcal{T}_{\text{Plate}} = 250\,\text{Myr}$ plate velocity period after an adjustment time of about 1 Gyr, while the plume period cannot adjust to a period of $\mathcal{T}_{\text{Plate}} = 125\,\text{Myr}$. Neither the plumes in (f) nor the pile thickness in (h) follow a 125 Myr cycle, which is represented in the short-wavelength variations of the pile edge postion (g). In contrast, the plume cycle has about the same period of 370 Myr as for a constant velocity of 1.48 cm/year (Figure 4b).

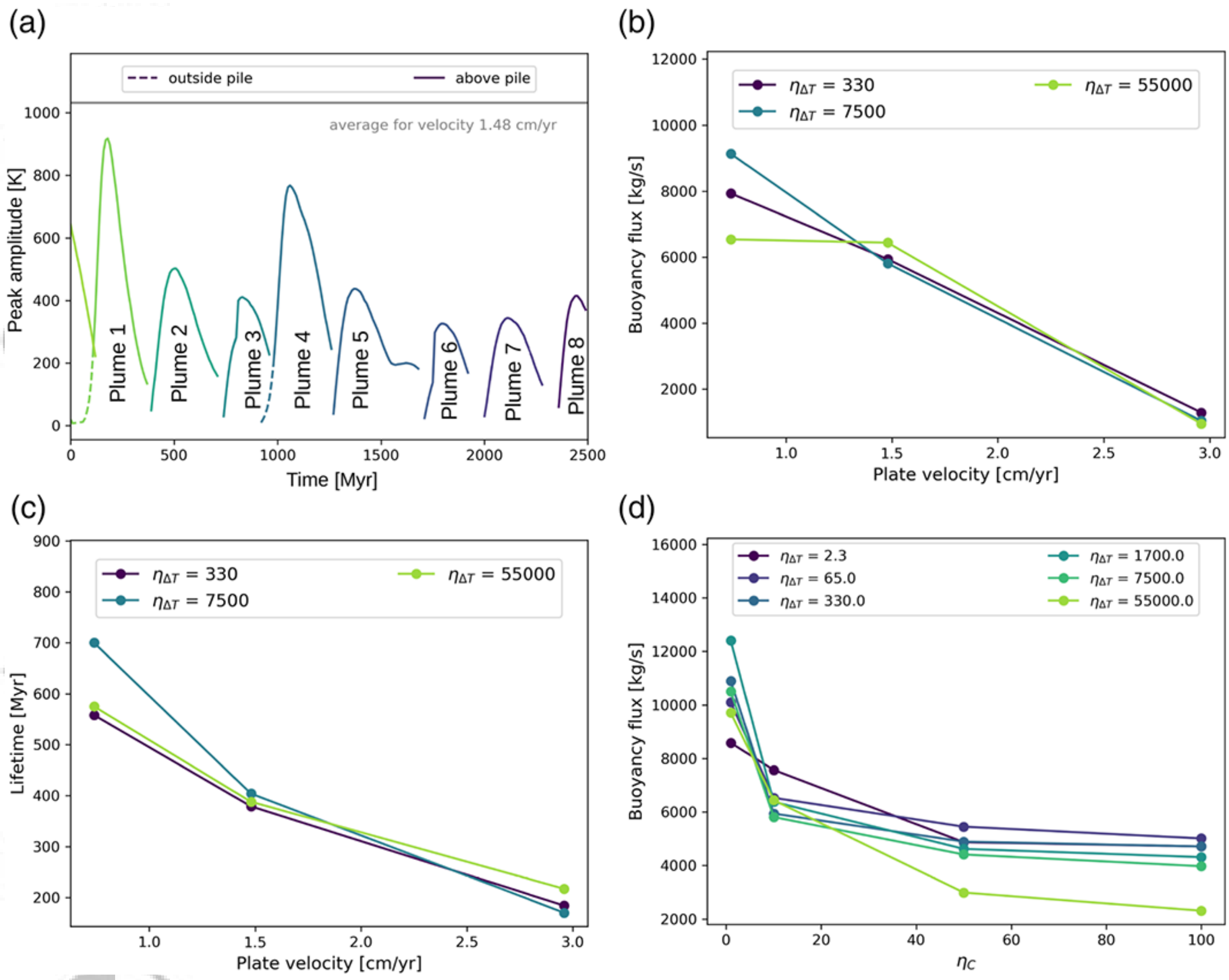

Figure 7. (a) Excess temperature of identified plumes at radius 4000 km for a model with $B = 0.8$, $\eta_C = 10$ and $\eta_{\Delta T} = 330$ and a constant plate velocity of 2.96 cm/year (increased compared to our reference model). Increased plate velocity not only reduces the excess temperature of plumes (compare (a) and Figure 4c), but also reduces plume lifetime (c) and buoyancy flux (b). Since the thermal boundary layer has less time to grow for a stronger TBL flow, plumes are weaker. This effect is independent of other parameters such as the temperature dependence $\eta_{\Delta T}$. (d) shows the buoyancy flux as a function of compositional viscosity contrast η_C for different values of thermal viscosity contrasts $\eta_{\Delta T}$. While there is no consistent variation of buoyancy flux with $\eta_{\Delta T}$, entrained dense material with higher η_C reduces the buoyancy flux by increasing the average plume viscosity. A similar reduction in buoyancy flux can also be observed for increased pile density B (not shown here).